Anisotropic Cellular Mechanoresponse for Radial Size Maintenance of Developing Epithelial Tubes

Tsuyoshi Hirashima*[1] and Taiji Adachi[2]

1. Department of Pathology and Biology of Diseases, Graduate School of Medicine, Kyoto University
2. Institute for Frontier Life and Medical Sciences, Kyoto University

Correspondence to:

Tsuyoshi Hirashima, Ph.D.

Department of Pathology and Biology of Diseases, Graduate School of Medicine, Kyoto University, Yoshida-konoe-cho, Sakyo-ku, Kyoto 606-8315, Japan.

Tel/Fax: +81-75-753-9450

E-mail: hirashima.tsuyoshi.2m@kyoto-u.ac.jp

Abstract

Cellular behaviors responding to mechanical forces control the size of multicellular tissues as demonstrated in isotropic size maintenance of developing tissues. However, how mechanoresponse systems work to maintain anisotropic tissue size including tube radial size remains unknown. Here we reveal the system underlying radial size maintenance of the murine epididymal tubule by combining quantitative imaging, mathematical modeling, and mechanical perturbations. We found that an oriented cell intercalation making the tubule radial size smaller counteracts a cell tension reduction due to neighbor cell division along the tubule circumferential axis. Moreover, we demonstrated that the tubule cells enhance actomyosin constriction driving the cell intercalation in response to mechanical forces anisotropically applied on the cells. Our results suggest that epididymal tubule cells have endogenous systems for responding as active cell movement to mechanical forces exclusively along the circumferential axis, and the anisotropic cellular mechanoresponse spontaneously controls the tubule radial size.

Keywords: Anisotropy; Epithelial tube; Mathematical model; Mechanoresponse; Quantitative imaging; Size maintenance; Tissue mechanics

Introduction

Cell-cell communication via cellular behaviors is necessary to regulate tissue maintenance, development, and size. The underlying principle for this communication is a cellular response produced in reaction to mechanical forces generated within the tissues [1,2]. In tissue volume maintenance, for example, cell proliferation is counterbalanced by cell death, and these coordinated cellular behaviors are the mechanoresponse to cell-crowding pressure due to proliferation, which leads to cell death within the tissue [3–5]. On the other hand, in tissue length maintenance along an axis, such as radial size maintenance of a tube during elongation [6–8], the anisotropic mechanoresponse system in tissues might organize cooperative cellular behaviors to distribute a net increase in the tissue volume not along the axis, but in other axes. However, the system responsible for this anisotropic tissue maintenance is unclear. Here we utilized epididymal tubules in murine embryo as an experimental model system for a proliferating single-layered epithelial tube [7,9] to reveal anisotropic cellular response to mechanical forces for radial size maintenance of proliferating tubes.

Results

Actomyosin constriction generated within epithelial cells is required for the maintenance of tubule radial size

In the epididymis, phosphorylated myosin regulatory light chain (pMRLC), a marker of active tension generation via actomyosin constriction, localizes only to apical cellular junctions of the epithelial tubules at 15.5 and E16.5 (Fig. 1A). To examine the mechanical roles of actomyosin constriction in the epididymal tubules, we applied Blebbistatin/Y-27632 for inhibiting actomyosin constriction of non-muscle myosin II [10,11] or Calyculin A for inhibiting the protein phosphatases of pMRLC [12] to the epididymides in explant cultures, and observed the tubule morphology 1 day after the inhibitor treatment (Fig. 1B). The inhibitor assay revealed that inhibiting actomyosin-mediated apical constriction resulted in tubule expansion whereas constitutive activation of the tension led to tubule shrinkage (Fig. 1B´; Materials and Methods (II-i)).

To clarify the inhibitor effects at the cell level, we examined morphological changes of the tubule cells by immunolabeling for the E-cadherin (Fig. 1C). For the Blebbistatin treatment as in the case of Y-27632, the tubule cells became flattened, i.e., those became more extended parallel to the tubule surface and the cell length along the apico-basal axis

68 became shorter than those in control. For Calyculin A treatment, each cell shape became
69 rounded due to strong cellular constriction, leading to the disintegration of cell-cell adhesion;
70 as a result of the aberrant constriction, some cells were excluded from the tubules and
71 lumenized structure of the epididymal tubules was disrupted (Fig. 1C).
72 For quantitative analysis at single cell resolution, we measured the cell height along the
73 apico-basal axis and the cell area at the middle point of the cell height, and calculated the cell
74 volume and the aspect ratio of cell shape as a measure for the cell flatness (Fig. 1D; Materials
75 and Methods (II-ii)). Interestingly, we found the cell volume was preserved even though the
76 aspect ratio became larger for the increase of tubule diameter in the case of Blebbistatin
77 treatment (Fig. 1D′). Based on this data, we performed mathematical analysis to examine
78 how the force balance in epithelial cells within mono-layered tissues influences the cellular
79 morphology at mechanical equilibrium and clarified that the cell area/height monotonically
80 increases/decreases for the attenuation of apical constriction (Materials and Methods (III-i)),
81 which can explain the variation of cell morphology for the inhibitor treatments. Taken
82 together, these results indicate that the force balance within the epithelial layer of the tubule
83 determines its radial size.
84
85 **Cell division along the circumferential axis of tubules produces mechanical forces to**
86 **expand the tubule**
87 Next, we examined the impact of cell division orientation in the tubule at E15.5 and E16.5
88 because the cell division orientation is a key determinant for the morphogenesis of
89 developing tubules [13,14]. We used phospho-histon H3 (pHH3) and γ-tubulin each as a
90 marker of mitotic cells and microtubule organizing centers (MTOCs). We measured spindle
91 orientation in the mitotic cells within the tubule by extracting the axis connecting between the
92 two MTOCs in each pHH3-positive cell without destructing the tissue structure (Fig. 2A-A”).
93 We manually measured three angles α_1 , α_2, and α_3 (Fig. 2B) to define a local coordinate
94 system *O*’ (Fig. 2C), origin of which corresponds to the center position of mitotic cell (white
95 arrows in Fig. 2B). In the local sphere coordinates, we obtained statistical distributions for
96 two angles of the cell division orientation: φ and θ (Fig. 2C; Materials and Methods
97 (II-iii)). The distribution of φ shows that most of the mitotic cells divide parallel to the
98 epithelial layer (The Rayleigh test, $P<0.001$ at E15.5 and E16.5); however, the distribution of
99 θ shows that the orientation is not biased towards the longitudinal or circumferential axis
100 (The Rayleigh test, $P>0.05$ at E15.5 and E16.5) (Fig. 2D). Furthermore, the distance between

101 MTOCs shows no correlations with the angle θ (r=-0.07 at E15.5, r=-0.02 at E16.5 where r
102 is the Pearson's correlation coefficient), denying a possibility that the spindle orientation
103 might turn to a specific orientation when the later stage of mitosis (Fig. 2E).
104 We then investigated how the cell division orientation affects the tubule morphology
105 using numerical simulations of a computational model (Mov. 1). We here employed the
106 vertex dynamics model, a type of cell-oriented model, to represent multi-cellular dynamics in
107 epithelial tubes [15–17]. See the Materials and Methods (III-ii) - (III-iv) for more details of
108 the mathematical model and simulation settings (Fig. S1). In the simulation, virtual epithelial
109 tubes grew along the division orientation, suggesting that cell division along the
110 circumferential axis is attributed to continuous radial growth (Fig. 2F and F′). In addition, we
111 found that the cell division orientation affects mechanical stress in each cell of the virtual
112 tubes (Fig. 2F). To evaluate the mechanical stress in the cells related to the tube
113 morphogenesis, we introduced a scalar quantity, i.e., cell tension anisotropy, which becomes
114 larger when the cell tension along the circumferential axis becomes weaker than that along
115 the longitudinal axis. See Eq. (v-2) in the Materials and Methods (III-v) for the definition of
116 cell tension anisotropy. As shown in Figure 2F-F′′, the cell tension anisotropy in the tubes
117 depends on the cell division orientation and corresponds with the growth direction of the
118 tubes. The simulation analysis indicates that the circumferential cell division leading to the
119 tube expansion entails the increase of cell tension anisotropy locally in the tissue. This
120 implies that cells should actively counteract the changes in cell tension anisotropy for tubule
121 radial size maintenance.
122
123 **Oriented cell intercalation and circumferential cell division should be coupled for the**
124 **maintenance of tubule radial size**
125 To explore how the cells react, we examined the pMRLC spatial distribution in the tubule at
126 sub-cellular resolution through automatic extraction for each apical cell junction (Fig. 3A).
127 We performed whole-tissue coimmunostaining for pMRLC and Zonula occludens-1 (ZO-1),
128 an apical tight junction marker, and quantified the pMRLC mean intensity at junctions,
129 junction angle, and length through digital image processing (Fig. 3B; Materials and Methods
130 (II-iv)). We found that the distribution of pMRLC intensity was well fitted to a log-normal
131 distribution (Fig. 3C), indicating that enriched pMRLC localization can be observed in an
132 unignorable number of apical junctions (Fig. 3D). To evaluate the relationship between the
133 junction angle and the pMRLC intensity, we categorized the junction angle into three groups;

134 longitudinal (long.): $0 \le \vartheta \le \pi/6$, intermediate (intm.): $\pi/6 < \vartheta < \pi/3$, and circumferential
135 (circ.): $\pi/3 \le \vartheta \le \pi/2$ (Fig. 3E). As shown in Figure 3E′, the pMRLC tends to localize more
136 on junctions that orient more in the circumferential axis (One-way ANOVA, P<0.001). As
137 well as the junction angle, we also categorized the junction length into three groups: short:
138 $0 \le \ell \le 2$ μm, middle: $2 < \ell < 4$ μm, long: $4 \le \ell \le 10$ μm (Fig. 3F), and found that the
139 pMRLC tends to localize more on shorter junctions (One-way ANOVA, P<0.001) (Fig. 3F′).
140 These results suggest that the circumferential junctions shrink through the
141 actomyosin-mediated constriction.
142 Because pMRLC localization on the apical junctions triggers cell intercalation mediated
143 through junction shrinkage [1,18], the polarized pMRLC localization on the circumferential
144 junctions can drive the oriented cell intercalation leading to longitudinal elongation and radial
145 shrinkage of the tubule. The present data suggest that the oriented cell intercalation causes the
146 tubule shrinkage; on the other side, the tubule expansion occurs due to the circumferential
147 cell division shown in the previous section. Therefore, the maintenance of tubule radial size
148 requires a proper balance between myosin activity driving intercalation and cell division
149 frequency.
150 To evaluate this relationship, we measured the pMRLC intensity along the tubule at the
151 whole organ scale at E15.5 and E16.5 (Materials and Methods (II-v)), and found that the
152 intensity in the head region of epididymis is larger than that in the tail region (Fig. 3G). This
153 intensity profile is similar to the spatial profile of the number of mitotic cells in the
154 epididymal tubules previously reported [19] (Fig. 3H). Indeed, the pMRLC intensity and the
155 mitotic cell numbers in the tubules show positive correlation (r=0.49 in E15.5 and r=0.56 in
156 E16.5 where r is the Pearson's correlation coefficient) (Fig. 3 H′; Materials and Methods
157 (II-vi)). Western blotting analysis also shows the myosin activity, defined as the ratio of
158 pMRLC to the total MRLC (tMRLC), in the head region is greater than that in the tail region
159 (Fig. 3I and I′). Moreover, cell morphology differences corroborate junctional tension due to
160 the pMRLC in each region (Fig. 3J and S2; Materials and Methods (II-vii)). The apical
161 junction length along the circumferential axis in the head region is shorter than that in the tail
162 region (Kruskal-Wallis test, P<0.001) (Fig. 3J′), and the apical surface area in the head
163 region are smaller than that in the tail region (Kruskal-Wallis test, P<0.001) (Fig. 3J′′). Thus,
164 a regulatory mechanism balancing the oriented cell intercalation driven by pMRLC
165 localization and cell division should exist.
166

Cell division provides mechanical stimulations to the neighboring cells

Cell division can generate mechanical perturbations in multi-cellular tissues [20]; hence, we anticipated that the cell divisions load the mechanical forces to the adjacent cells of divided ones and this stimulus would trigger the oriented cell intercalation in the epididymal tubule. We then investigated the change of the cell tension anisotropy against the cell division using extensive numerical simulations of the vertex dynamics model.

We examined the dependency of cell division anisotropy against the two factors: relative position of cells to the neighbors cell division axis (Fig. 4A) and normalized elapsed time from the cell division $\tau_\alpha'^{\text{cycle}}$, ranged from 0 to 1 (see the Materials and Methods (III-iv) for the definition). In addition, we focused on the two cases of cell division orientation, i.e., longitudinal ($0 \le \theta \le \pi/6$ where θ is defined in Fig. 2C) and circumferential ($\pi/3 \le \theta \le \pi/2$), and made histograms of the cell tension anisotropy for each case (Fig. 4B). The results shown in Figure 4B′ indicate that the cell division mechanically affects the cell tension anisotropy in the neighboring cells of divided cells on the division axis (Rows in Fig. 4B′). This is intuitive because the divided cells push along the division axis to the neighboring cells and hence, tension in the neighboring cells along the division axis can be attenuated. Furthermore, the histograms show that the attenuation effect due to the cell division becomes smaller along with the elapsed time from the cell division $\tau_\alpha'^{\text{cycle}}$. (Columns in Fig. 4B′).

Would the cell division be the only source to produce the tension attenuation of cells within multicellular tissues? To answer this question, we next plotted histograms of the elapsed time from the cell division $\tau_\alpha'^{\text{cycle}}$ when the cell tension anisotropy ρ_α is over various thresholds $\rho^* = 0.039,\ 1,$ and 0.2 in the cells on the circumferential axis of divided cells (Fig. 4C-C′′; $\rho^* = 0.0385$ is the mean of cell tension anisotropy in the upper left case of Fig. 4B′). Our numerical investigations revealed that the cell tension anisotropy could become over the given thresholds at timing elapsed enough from the cell division although the cell tension anisotropy in most of the cells (~70%) are affected immediately following to the cell division.

These results led to the two conclusions. First, most of the cells that receive significant mechanical impact from the cell division should be on the cell division axis and can be found soon after the cell division. Second, cell tension can be varied independent to the cell division,

198 rationalizing the introduction of mechano-responsive regime into our model argued in the
199 later section.
200
201 **Mechanical stimulations provided by neighbor cell divisions trigger the onset of cell**
202 **intercalation**
203 To directly observe cellular responses to the mechanical forces generated by the cell divisions,
204 we performed live imaging analysis for epididymal tubule cells dissected at E15.5 using ex
205 vivo organ culture systems. For visualization of the tubule cell membrane, a conditional
206 fluorescence reporter line, crossed the R26R-Lyn-Venus line [21] and the Pax2-Cre line [22],
207 was used. Because the epididymal tubules were located in deep region of the epididymis,
208 ~100 μm away from the capsule of epididymides (Fig. 5A), confocal microscopy was not
209 appropriate for this case; hence, we employed an incubator-integrated multiphoton excitation
210 microscope system for stable deep tissue live imaging in explant cultures (Fig. 5B).
211 We focused on the behavior of cells neighboring to mitotic cells on the cell division axis
212 as those cells are more likely to show cellular responses against the mechanical perturbations
213 according to the first conclusion in the previous section. Careful observations led to the
214 discovery of characteristic behaviors in those cells; the oriented cell intercalation for
215 elongating the tubule occurs more frequently against the circumferential cell division
216 compared against the longitudinal one (Fig. 5C and Mov. 2). For quantification of the
217 oriented cell intercalation behavior, we measured the cell intercalation strain rate [23] for the
218 circumferential ($0 \le \theta \le \pi/6$) or longitudinal cell division ($\pi/3 \le \theta \le \pi/2$) (Fig. 5C and S3),
219 and calculated the cell intercalation rate for tube elongation (CITE) as a measure of the
220 oriented cell intercalation in the tubules. Positive/negative values of the CITE indicate that
221 cell intercalations undergo for the tubule elongation/shortening (Fig. 5D; see the Materials
222 and Methods (II-viii) for more details of CITE). From the quantitative analysis, we found that
223 the oriented cell intercalation tends to occur 60 min after the circumferential cell division
224 (*t*-test $P<0.05$ in the time range: 50-60 min in the case of circumferential cell division) (Fig.
225 5E).
226 Considering the cellular movement as an output response, the oriented cell intercalation
227 should be operated through rapid biochemical process such as phosphorylation. In addition to
228 this inference, we demonstrated by the extensive numerical simulations that the cell division
229 within the epithelial tissues could attenuate the cell tension in adjacent cells along the
230 division orientation owing to pressure of the dividing cells to the adjacent ones (Fig. 2F and

4B′). Therefore, we hypothesized that MRLC would be phosphorylated as a cellular response to the reduction of circumferential cell tension provided by the neighboring cells, ultimately driving the oriented cell intercalation.

Polarized cellular responses to mechanical simulations lead to the maintenance of the tubule radial size

To check whether this hypothesis is rational, we carried out the computer simulation of the vertex dynamics model including a mechano-responsive regime and its counterpart regimes (Mov. 3). We implemented the mechano-responsive regime into the mathematical model as the cells keep constricting one of the circumferential junctions for a parameterized period since the cell tension anisotropy ρ_α reached at the threshold value ρ^* due to the reception of intense pressure (Fig. 6A and S4; Materials and Methods (III-v)). Through the numerical analysis, we found that the mechano-responsive regime in the simulation realized spatiotemporally-constant tubes with smaller radial size compared to the case of no regulation (Fig. 6B and D).

On the other hand, we performed simulations in counterpart regime, the 'scheduled' regime, where the timing for junction constriction was predetermined and the constricting cells were randomly selected. For determining the schedule of the constriction, we sampled the ratio of constricting cells along the course of normalized simulation time τ' in the mechano-responsive regime and obtained the function by fitting the mean curve data (Fig. 6C; see Eq. (v-3) in the Materials and Methods (III-v)). In the scheduled regime, the simulation generated tubes with irregular surfaces and non-constant radial size along the longitudinal axis whereas the radial size was smaller as well as the case of mechano-responsive regime (Fig. 6B, D and D′).

In the scheduled regime, the oriented cell intercalation that leads to the local shrinkage of tubules occurs independently to the variations of cell tension, resulting in the irregular surface of tubules. In the mechano-responsive regime, however, the mechanical stress at the supra-cellular scale can be modulated due to the active multicellular movement immediately responding to the mechanical perturbations; therefore, the smooth-curved surface throughout the longitudinal axis of tubules can be realized in this regime. These simulation analyses suggest that the mechano-responsive regime, as an embodiment of our hypothesis, explain the radial size maintenance of proliferating tubes.

The epididymal tubule cells exhibit cellular responses as myosin activation to anisotropic mechanical perturbations

To verify the hypothesis, we applied uniaxial compression to isolated epididymides embedded in collagen gel using a flexible polydimethylsiloxane (PDMS) chamber, and evaluated the myosin activity as a cellular response to the compression (Fig. 7A). We performed the compression assay for 3 groups, i.e., no uniaxial compression as the control, lateral, and longitudinal compression, to examine the cellular response to different mechanical perturbations (Fig. 7B). After 10 min of continuous load, we quantified the cell shape and configuration altered to the uniaxial compression. For the quantification, we extracted the shape of epididymal cells from the immunofluorescence images for E-cadherin (Fig. 7C), and calculated the aspect ratio and the major axis angle from best-fit ellipses of the cell shapes. The shape and configuration of cells in the uniaxial compression treatments were significantly different from those in the no uniaxial compression, confirming that the epididymal tubule cells were deformed along the compression axis (The Kruskal-Wallis test, $P<0.001$) (Fig. 7D-D′′).

After 20 min, we measured the myosin activity as the relative intensity of pMRLC to the total MRLC (tMRLC) and found that the myosin activity is larger in the lateral compression compared in other cases, indicating that the MRLC phosphorylation is exclusively enhanced due to the lateral compression (The Friedman test, $P<0.05$) (Fig. 7E and E′). Moreover, we quantified the level of MRLC kinase as the ratio of the Rho-associated protein kinase 1 (ROCK1) to the tMRLC, and found that it was not significantly different between treatments (The Friedman test, $P>0.05$) (Fig. 7E and E′′). These results suggest that the epididymal tubule cells possess an intrinsic system in which MRLC phosphorylation is triggered in response to the cell tension reduction along the tubule circumferential axis without changing the total amount of ROCK.

Discussion

Altogether, we showed that the cells trigger myosin activation leading to oriented cell intercalation by responding to mechanical forces anisotropically in the tubule. Therefore, we propose a system in which the spontaneous mechanoresponsive behavior of cells at the supra-cellular scale organizes the maintenance of the tubule radial size at the tissue scale (Fig. 4F). In developmental processes, anisotropic growth of proliferating tissues while

maintaining an axis, such as tube elongation due to the radial maintenance specifically dealt with in this study, causes generation of compressive forces in the growing axis, eventually leading to a buckling-induced wavy pattern formation [7,24,25]. Thus, the proposed polarized mechanoresponse system might work as a regulatory principle underlying mechanisms for self-organized tissue morphogenesis [26,27].

To understand the system further, future work will need to identify what molecular machineries sense the anisotropic mechanical force in tissues and how the received mechanical stimuli are chemically transduced to activate the myosin in apical junctions. It is tempting to speculate that the directional preference of cells would be provided by regulators of planar cell polarity (PCP) that promote the downstream myosin phosphorylation [1,28,29], such as Vang-like (VANGL) and Tyrosine-protein kinase-like 7 (PTK7). These proteins are well aligned circumferentially in junctions of epididymal tubule cells and loss of PCP disrupts the actomyosin-mediated cell intercalation resulting in tubule expansion [30] (Fig. S5) as seen in kidney development [6]. Our findings reveal structural components and dynamic properties in the mechanoresponse system that controls tissue morphogenesis.

Materials and Methods

This section includes (I) Experiments, (II) Quantifications, (III) Mathematical modeling, and (IV) Others (Statistical tests, etc.).

(I) Experiments

(i) Animals

For live imaging analysis, we used fluorescence reporter mice produced by crossing the Pax2-Cre line[22] (a gift from T. Furukawa in Osaka Univ.) and R26R-Lyn-Venus line[21]. Otherwise, we used imprinting control region (ICR) mice purchased from Japan SLC, Inc. We designated the midnight preceding the plug as embryonic day 0.0 (E0.0), and all mice were sacrificed by cervical dislocation to minimize suffering at E15.5 or E16.5. All the animal experiments were approved by the local Ethical Committee for Animal Experimentation of Institute for Frontier Life and Medical Sciences, Kyoto University, and were performed in compliance with the Guide for the Care and Use of Laboratory Animals at Kyoto University.

(ii) Antibodies and Fixative Solutions for Immunostaining

We used the following primary antibodies with dilution ratio 1:200 as a standard condition: rabbit monoclonal anti-E-cadherin (Cell Signaling Technology, #3195), mouse monoclonal anti-γ-Tubulin, (Sigma-Aldrich, #5326), rabbit polyclonal anti-phospho histon H3 (pHH3)(Merck Millipore, #06-570), rat monoclonal anti-pHH3 (Abcam, #ab10543), rabbit polyclonal anti-phosho Myosin light chain (pMRLC) (Abcam, #ab2480), rabbit polyclonal anti-Vangl1 (Atlas Antibody, #HPA025235), goat polyclonal anti-Vangl2 (Santa Cruz Biotechnology, #sc-46561), and mouse monoclonal anti-ZO-1 (Thermo Fischer Scientific, #33-9100). We used the paraformaldehyde (PFA) for anti-E-cadherin, anti-γ-Tubulin, and anti-pHH3; we used the trichloroacetic acid (TCA) for anti-pMRLC, anti-Vangl1, anti-Vangl2, and anti-ZO-1.

(iii) Whole-tissue Immunofluorescence and Fluorescent Dye

Dissected epididymides were fixed with 4% PFA in phosphate buffered saline (PBS) for 2 h at 4°C or for 20 min at 37°C, or with 2% TCA in Ca^{2+}- and Mg^{2+}-free PBS for 20 min at 4°C, depending on target epitopes. The samples were then blocked by incubation in 10% normal goat serum (NGS) (Abcam, #ab156046) or 10% normal donkey serum (Abcam, #ab166643)

346 diluted in 0.1% Triton X-100/PBS, depending on derived animals of secondary antibody, for
347 3 h at 37°C. The samples were treated with primary antibodies overnight at 4°C, and
348 subsequently incubated with secondary antibodies conjugated to either the AlexaFluor 546 or
349 the AlexaFluor 647 (1:1000, Thermo Fischer Scientific) overnight at 4°C. We used
350 TRITC-conjugated phalloidin (0.3 μg/ml, Merck Millipore, #FAK100) and Hoechst 33342 (5
351 μg/ml, Thermo Fischer Scientific, #H3570) for the visualization of F-actin and DNA,
352 respectively.
353
354 **(iv) Volumetric Fluorescence Imaging**
355 We mounted samples with 1% agarose gel of 10 μl on a glass-based dish (Greiner Bio-One,
356 #627871) for stable imaging. Then, the samples were immersed with the BABB solution
357 (benzyl-alcohol and benzyl-benzoate, 1:2) or CUBIC2 solution for optical clearing[19,31,32].
358 Finally, we obtained 8-bit volumetric fluorescence images using the confocal laser scanning
359 platform Leica TCS SP8 equipped with the hybrid detector Leica HyD. We used the
360 objective lenses magnifications of ×20 (numerical aperture (NA) = 0.75, working distance
361 (WD) = 680 μm, HC PL APO CS2, Leica), ×40 (NA = 1.3, WD = 240 μm, HC PL APO CS2,
362 Leica), or ×60 (NA = 1.4, WD = 140 μm, HC PL APO CS2, Leica).
363
364 **(v) Explant Organ Culture**
365 The epididymides were surgically excised at a region of the vas deferens close to the tail of
366 epididymis, and those with testis were dissected from the embryonic body. Samples were
367 then placed on a hydrophilic polytetrafluoroethylene organ culture insert with a pore size of
368 0.4 μm (Merck Millipore, #PICM01250), which was preset in a 35 mm petri dish (Thermo
369 Fischer Scientific, #153066) filled with a culture medium. The culture medium we used was
370 Dulbecco's Modified Eagle's medium (Nacalai Tesque, #08489-45), containing 10% fetal
371 bovine serum (Thermo Fischer Scientific, #12483) and 1% penicillin-streptomycin mixed
372 solution (Nacalai Tesque, #26253-84) at 37°C under 5% CO_2. The samples were cultured in
373 an air-liquid interface; the total amount of culture medium was 800 μl for the petri dish.
374
375 **(vi) Small-molecule Inhibitors**
376 We used the following inhibitors to suppress or activate the generation of
377 actomyosin-mediated tension: Blebbistatin (Merck Millipore, #203391), Y-27632 (Merck
378 Millipore, #SCM075), and Calyculin A (Cell Signaling Technology, #9902).
379

380 **(vii) Live Imaging**

381 The organ culture setting was according to the condition as described above with the
382 following 2 minor modifications. First, we used a 35 mm glass-based dish (Iwaki,
383 #3910-035) with 700 μl of the culture medium in the dish. Second, we adhered each
384 supporting leg of the organ culture insert on the dish with 20 μl of 1% agarose gel. This
385 preparation prevents the culture insert from sliding during the live imaging. We used an
386 incubator-integrated multiphoton fluorescence microscope (Olympus) using a ×25
387 water-immersion lens (NA = 1.05, WD = 2mm, Olympus). Imaging conditions were as
388 follows; excitation wavelength: 945nm (Mai-Tai DeepSee eHP, Spectra-Physics), AOTF:
389 3.5%-1.5%, scan size: 1024 × 320 pixels, scan speed: 10 μsec/pixel, z-axis interval: 1 μm,
390 and time interval: 5 min, magnification: ×2.

391

392 **(viii) Tissue Compression Assay**

393 For the tissue compression assay, we used a manual stretch/compression device (STREX,
394 #STB-10) with a polydimethylsiloxane (PDMS) chamber (STREX, #STB-CH-04), and
395 conducted in the following manner. First, we exposed the PDMS chamber to plasma arc for 1
396 min using a desktop vacuum plasma processing device (STREX, PC-40) for hydrophilic
397 treatment to enhance the adhesion between the chamber and collagen gel into which the
398 epididymides were embedded. Next, we immediately placed isolated epididymides onto the
399 hydrophilized PDMS chamber in its 50% stretched state, and fulfilled with 500 μl of type I
400 collagen (Nitta Gelatin, Cellmatrix Type I-A), followed by gelation process for 10 min at
401 37°C. Then, we applied 1 ml of the culture medium into the chamber, and the epididymides
402 with the collagen gel were compressed by relaxing from the 50% stretched state around 0.2
403 mm/sec. No relaxing the stretched chamber was regarded as control treatment. Finally, the
404 samples were incubated for 10 min for the morphological confirmation analysis and 20 min
405 for the Western blotting analysis at 37°C under 5% CO_2. In the lateral compression assay, the
406 epididymal tubules were deformed along the circumferential axis in any peripheral region
407 and the circumferential length of individual cells became smaller. We consider this is due to
408 gravity of the culture medium filled on the upper layer of gel as this does not happen without
409 the culture media.

410 For the immunoblotting assay, we extracted total protein from each treatment, and
411 adjusted the amount to the same among the treatments for the SDS-PAGE as described above.
412 We first confirmed that there were no significant differences of GAPDH and those of MRLC
413 among the treatments. Then, we evaluated the myosin activity and the level of MRLC kinase

414 (ROCK1); even when the ROCK1 level in the epididymides was evaluated as the ratio of
415 ROCK1 to the GAPDH, it showed qualitatively the same results. There was no ROCK2
416 expression in the epididymides. Finally, the activities were each normalized by mean values
417 of the control group.
418
419 **(ix) Total Protein Extraction and Western Blotting**
420 For total protein extraction, dissected epididymides were immersed in the SDS-free RIPA
421 buffer with protease inhibitor cocktail (Nacalai Tesque, #08714) supplemented with the
422 EDTA-free phosphatase inhibitor cocktail (1:100, Nacalai Tesque, #07575), and were
423 disrupted by an ultrasonic cell disruptor (Microson). The lysates were placed onto the ice for
424 20 min and were centrifuged at 13,000 ×g for 10 min at 4°C. Protein concentration of the
425 supernatant was determined by the bicinchoninic acid assay.
426 The lysates were prepared for SDS-PAGE by adding 2×Laemmli sample buffer
427 (Bio-Rad, #161-0737) with 2-mercaptoethanol (Bio-Rad, #161-0710) and by boiling at 96°C
428 for 5 min. Next, the lysates containing approximately 5 μg of proteins were loaded into each
429 lane of the Mini-PROTEAN precast gels (Bio-Rad, #4569035), and electrophoresis was
430 carried out in Tris/glycine/SDS running buffer (Bio-Rad, #1610732) at constant 150V for 35
431 min. Then, the proteins were blotted onto 0.2 μm polyvinylidene difluoride membrane
432 (Bio-Rad, #1704272) in HIGH MW mode (1.3A, 25V for 10 min) of the Trans-Blot®
433 Turbo™ Transfer System (Bio-Rad, #170-4155) for ROCK1 detection and in the LOW MW
434 mode (1.3A, 25V for 5 min) for others.
435 The blotted membranes were then immersed in 15% H_2O_2/Tris-buffered saline (TBS)
436 solution for 30 min at room temperature for blocking endogenous peroxidase followed by
437 blocking with 5% NGS at 37°C for 60 min. For immunoblotting, the membranes were
438 incubated with primary antibodies diluted in 0.1% TBS/Tween-20 at 4°C over night. The
439 concentrations of antibodies used were 1:100,000 for mouse monoclonal anti-GAPDH (Wako,
440 #015-25473), 1:500 for rabbit polyclonal anti-myosin light chain 2 (Cell Signaling, #3672)
441 and mouse monoclonal anti-phospho-myosin light chain 2 (Cell Signaling, #3675), and
442 1:2000 for rabbit monoclonal anti-ROCK1 (Abcam, #ab45171). Then, the membranes were
443 incubated with diluted secondary antibody solutions in TBS/Tween-20 at 37°C for 60 min;
444 the concentration was 1:50,000 for goat anti-rabbit IgG conjugatd to horseradish peroxidase
445 (HRP) (Santa Cruz Biotechnology, sc-2004) and goat anti-mouse IgG conjugated to HRP
446 (Santa Cruz Biotechnology, sc-2005). Finally, protein bands were detected using the
447 Amersham ECL Select Western Blotting Detection Reagent (GE Healthcare, #RPN2235),

448 and were scanned with ImageQuant LAS 4000 (GE Healthcare).
449
450
451 ## (II) Quantifications
452 **(i) Tubule Diameter in Inhibitor Assay (Fig. 1B and B')**
453 First, we performed immunostaining for the E-cadherin of 8 different epididymides for each
454 inhibitor treatment to visualize the epididymal tubule as described above, and obtained the
455 volumetric images of 512 × 512 pixels using ×20 lens with z-axis interval of 5 μm. We
456 utilized the built-in module of a software platform, the Leica Suite X, (Leica), to create a
457 montage image of whole epididymis. Then, we manually extracted epididymal tubules from
458 maximum intensity projection images by erasing the efferent ductules and noise pixels due to
459 non-specific staining. From the preprocessed images, we obtained the centerline of
460 epididymal tubule by applying the built-in skeletonization algorithm in MATLAB for the
461 binary images obtained with arbitrarily determined thresholds, and finally calculated the
462 diameter along the centerline of tubule.
463
464 **(ii) Aspect Ratio and Cell Volume in Inhibitor Assay (Fig. 1C-D')**
465 First, we performed immunostaining for the E-cadherin of dissected epididymides to
466 visualize shape of individual epididymal cells as described above, and obtained the
467 volumetric images of 512 × 512 pixels using ×40 lens with z-axis interval of 1 μm. We
468 collected all samples from 3 different epididymides for each treatment. Then, we chose a
469 sampling point along the centerline of an epididymal tubule randomly, and collected 5
470 samples for the cell height and 20 cell samples for the characteristic cell length along the
471 circumferential direction of the epididymal tubule. For each sampling point, we manually
472 measured the cell height on an image plane that exposed the apical-basal axis of the cells
473 (right column of the Fig. 1C). In addition, we manually traced peripheral of the cells at the
474 middle point of cell height and measured cell area (left column of the Fig. 1C); we then
475 calculated the square root of the cell area for the characteristic length of the cells. Note that
476 the cell areas at any point of the cell height are not significantly different from those at
477 apical/basal sides. Utilizing the cell height and the characteristic length, we finally calculated
478 the aspect ratio between the two measures as defined in Fig. 1D, and the cell volume by the
479 multiplication of the two. Because the values of cell height are almost same within each
480 sampling point, we used only the mean value of cell height for the calculation of the aspect

481 ratio and that of the cell volume. Therefore, the standard deviations for the aspect ratio and
482 the cell volume represent the variations in the characteristic cell length.
483
484 **(iii) Cell Division Orientation (Fig. 2A-D)**
485 We first performed coimmunolabeling for γ-Tubulin and pHH3 of 6 different epididymides
486 to detect microtubule organizing centers of mitotic cells as described in this section (I)-(iii)
487 with a minor modification. That is, the samples were incubated in 10 mM sodium citrate
488 buffer including 0.1% Triton X-100/PBS for 20 min at 80°C for heat-induced retrieval of
489 γ-Tubulin epitope before blocking treatment. Next, we obtained volumetric images of 1024 ×
490 256 pixels as described above using ×40 lens with z-axis interval of 1 μm. Third, we
491 manually measured three angles α_1, α_2, and α_3 shown in Fig. 2B for each mitotic cell to define
492 a local coordinate system (*O*'; see Fig. 2C), origin of which corresponds to the center position
493 of mitotic cell. Each orthogonal basis of *O*'-coordinate is defined as follows: longitudinal
494 direction of epididymal tubule (*x*'), surface normal of epididymal tubule (*z*'), and orthogonal
495 direction for both *x*' and *z*' according to the right-handed system (*y*'). Then, we manually
496 measured positions of the two γ-Tubulin-positive dots (microtubule organizing centers:
497 MTOCs) in a pHH3-positive cell, and obtained two angles φ and θ in a local sphere
498 coordinate (Fig. 2D) resulted from coordinate transformation into the *O*'-system. Finally, we
499 selected samples under a criterion that the distance between the two γ-Tubulin-positive dots
500 is more than 1.5 μm. We regarded the samples whose φ is less than 40 degree as cells
501 dividing in parallel to the surface of epididymal tubule.
502
503 **(iv) Apical Junction Morphology and pMRLC/VANGL Signal Intensity (Fig. 3A-F', Fig.**
504 **S2, and Fig. S5)**
505 We performed coimmunostainining for ZO-1 and either pMRLC or VANGL2 of 8 different
506 epididymides as described above with a minor modification: the dilution ratio of
507 anti-pMRLC was 1:400 for preventing saturation binding. We obtained volumetric images of
508 1024 × 256 as described above using ×60 lens with z-axis interval of 0.3 μm. Then, we
509 separated the images into smaller ones around 200 pixels (≈36 μm) on a side so that the slope
510 of epididymal tubule can be regarded as a linear line.The longitudinal The digital image
511 processing was performed as follows. First, images for ZO-1 were filtered slice by slice with
512 a 2D median filter (3 × 3 pixels) followed by a 3D Gaussian filter with a standard deviation
513 of 3 pixels to reduce undesired noise. Next, the filtered images were binarized using the 3D

514 maximum entropy thresholding method [33], and the maximum one among the binarized
515 component of 26-connected pixels was regarded as an apical junction network. Then, we
516 performed 3D skeletonization process for the images of apical junctions, and obtained a
517 graph network including nodes and edges of skeletonized voxels utilizing distributed
518 MATLAB codes with modifications [34]. Finally, to extract the skeleton of apical cellular
519 junctions (Fig. 3A), we screened out the skeletonized edges to avoid over-skeletonization
520 results in the following 3 criteria; (1) The edge length between two nodes is less than 10 μm,
521 (2) the edge length is shorter than two-fold linear length between two nodes linked with the
522 corresponding edge, (3) the number of edges from a node is more than 3. The screening
523 process under the criteria produced 96% left from the total number of raw skeletonized edges.
524 The relative angle of apical junction edges against the longitudinal axis of epididymal tubule
525 was calculated as $\vartheta_j = \left|\cos^{-1}\left(\hat{\mathbf{g}}_j \cdot \hat{\mathbf{l}}\right)\right|$ where j is an index of apical edges, $\hat{\mathbf{g}}$ is an unit
526 vector of apical edges, and $\hat{\mathbf{l}}$ is that of the longitudinal axis of tubule, as shown in Figure
527 3B. For the signal quantification, we extracted signal intensity of pMRLC or that of
528 VANGL2 on the apical cellular junctions by using a thickened skeleton of apical junctions
529 with a dilation operator (3 × 3 × 3 voxels), and calculated average values for each edge of
530 thickened apical junction skeletons.
531
532 **(v) pMRLC Signal Intensity along Epididymal Tubule (Fig. 3G and H)**
533 First, we performed immunostaining for the pMRLC of 12 different epididymides as
534 described above with a minor modification: the dilution ratio of anti-pMRLC was 1:100.
535 Second, we obtained the volumetric images of 512 × 512 as described above using ×20 lens
536 with z-axis interval of 1 μm; we manually made montage images to avoid an overlap region
537 of composite images. Third, we manually erased signal intensity on pixels corresponding to
538 non-apical cellular region from the MIP images to obtain the centerline of epididymal tubule
539 as described above. Then, we calculated average values of pMRLC intensity within a circle
540 with a radius of 9 um along the epididymal tubule. Finally, we obtained the pMRLC signal
541 distribution along the epididymal tubule by smoothing the averaged signal intensity with a
542 moving average filter with a span of 40 μm – data in 20 μm range from the both ends of
543 tubule were omitted. The maximum value of vertical axis in Fig. 3H is 1 which corresponds
544 to the maximum intensity of 8 bit images. The horizontal axis of Fig. 3H was normalized by
545 the tubule length of each sample.
546

547 **(vi) Correlation between the Number of Mitotic Cells and pMRLC Signal Intensity (Fig.**
548 **3H')**
549 We used the data on the number of mitotic cells from our previous work [19] and one on the
550 pMRLC intensity obtained in this study. We divided 30 bins along the epididymal tubule and
551 calculated maximum likelihood estimates with the Poisson distribution for the number of
552 mitotic cells and with the Gaussian distribution for the pMRLC intensities in each bin. The
553 Pearson's correlation coefficients are 0.49 (P-value=0.006) for E15.5 and 0.56
554 (P-value=0.001) for E16.5.
555
556 **(vii) Apical Surface Area (Fig. 3J and 3J")**
557 We obtained 1024 × 256 volumetric images of fluorescently-labeled F-actin in epididymal
558 tubules as described above using ×40 lens with z-axis interval of 1 μm, and randomly
559 collected samples of apical cell surface from image planes of 3 different epididymal
560 volumetric data on which the apical cell surfaces exhibited. Then, we calculated the apical
561 surface area by tracing the peripheral of apical cell surfaces manually.
562
563 **(viii) Cell Intercalation Rate for Tube Elongation (CITE)**
564 We first obtained time-lapsed volumetric images for epithelial dynamics from the head
565 region of 4 different samples at E15.5 through the live imaging as described above, and
566 collected time series data for a group of cells around mitotic cells. In particular, we sampled
567 those cells on an image plane perpendicular to the optical axis from the image data, and
568 focused on cross sections in-between the apical and basal part of cells. We defined
569 cytokinesis as an origin of time for our analysis, and analyzed data on cell intercalation
570 dynamics with time interval of 10 min ($\Delta t = 10\,\mathrm{min}$).
571 Next, based on an earlier study, we calculated the cell intercalation strain rate tensor $\mathbf{L}_\mathbf{I}^t$
572 at time t as follows:
573 $$\mathbf{L}_\mathbf{I}^t = \mathbf{L}_\mathbf{T}^t - \mathbf{L}_\mathbf{C}^t,$$
574 where $\mathbf{L}_\mathbf{T}^t$ is a local tissue velocity gradient tensor, and $\mathbf{L}_\mathbf{C}^t$ is a cell shape strain rate tensor
575 [23]. Because our analysis was performed in planar, the tensors are 2 × 2 matrices. For the
576 calculation of a local tissue velocity gradient tensor $\mathbf{L}_\mathbf{T}^t$, we specified one or two neighboring
577 cells of a daughter cell from a mitotic cell that located an extension of the division axis as
578 central cells, and marked the adjacent cells of the central cells including the central cells and
579 the daughter cell as domain cells. Then, we manually traced each one of n domain cells to

obtain cell areas, cell shapes with the best fit ellipses, and cell centroids $\mathbf{r}_j^t$, where j is an index of domain cells (see marked cells by yellow lines in Fig. S4A). Using data of the cell centroids $\mathbf{r}_j^t$ and that of velocities $\mathbf{u}_j^t$, the local velocity gradient tensor was obtained by the least squares approximations according to the following equation,

$$\mathbf{u}_j^t \approx \left\langle \mathbf{u}^t \right\rangle + \mathbf{L}_{\mathrm{T}} \left(\mathbf{r}_j^t - \left\langle \mathbf{r}^t \right\rangle \right),$$

where $\left\langle \mathbf{r}^t \right\rangle = \sum_j \mathbf{r}_j^t / n$, $\mathbf{u}_j^t = \left(\mathbf{r}_j^{t+\Delta t} - \mathbf{r}_j^t \right) / \Delta t$ and $\left\langle \mathbf{u}^t \right\rangle = \left(\left\langle \mathbf{r}^{t+\Delta t} \right\rangle - \left\langle \mathbf{r}^t \right\rangle \right) / \Delta t$. $\langle \cdot \rangle$ indicates an average within the domain.

For the calculation of the cell shape strain rate tensor $\mathbf{L}_{\mathbf{C}}^t$, we used lengths of principal axes of a fitted ellipse and angle of the major axis from the longitudinal axis of epididymal tubule to obtain a matrix $\mathbf{C}_j^t$ that represents the cell ellipse. Then, we calculated $\mathbf{L}_{\mathbf{C},j}^t$ from $\mathbf{C}_j^t$ and $\mathbf{C}_j^{t+\Delta t}$, and $\mathbf{L}_{\mathbf{C}}^t$ was calculated by taking the area-weighted average of $\mathbf{L}_{\mathbf{C},j}^t$ within the domain cells. Note that we normalized $\mathbf{L}_{\mathbf{C}}^t$ to satisfy that a trace of $\mathbf{L}_{\mathbf{C}}^t$ was equal to that of $\mathbf{L}_{\mathbf{T}}^t$, realizing that the cell intercalation strain rate tensor $\mathbf{L}_{\mathbf{I}}^t$ had zero dilation.

Finally, we obtained the CITE at time t (L_{ll}^t) from an element of the cell intercalation strain rate tensor:

$$\mathbf{L}_{\mathbf{I}}^t = \begin{pmatrix} L_{ll}^t & L_{lc}^t \\ L_{cl}^t & L_{cc}^t \end{pmatrix}.$$

Note that the $L_{ll}^t = -L_{cc}^t$.

The data were classified into two groups depending on the relative angle of cell division axis to the longitudinal axis of epididymal tubule – we defined the relative division angle of 0-30 degrees as longitudinal division and that of 60-90 degrees as circumferential division.

(III) Mathematical Modeling

(i) Mathematical Analysis for Tube Morphology at Mechanical Equilibrium in Inhibitor Assay (Fig. 1D)

We here argue a point that the results in the inhibitor assays can be explained by mechanical force balance in the tubule tissue. To do so, we defined a potential energy of single epithelial cells in tissues based on our experimental results, and analyzed how actomyosin-based

608 constriction on apical junctions affects epithelial morphology at mechanical equilibrium. We
609 referred to an earlier study [35] for the analysis in this section. The following notations are
610 valid only in this subsection.

611 We considered an epithelial sheet, each cell within which has the volume V and
612 adheres neighboring cells with the area *S*. Each single cell generates contractile forces at the
613 apical junctions whose perimeter P. Then, we defined the potential energy as a minimum
614 form from the epithelial morphology as follows:

615 $$U_{\mathrm{Cell}} = \lambda_{\mathrm{Adh}} S + \lambda_{\mathrm{P}} P^2 + \lambda_{\mathrm{V}} \left(V - V_0\right)^2, \qquad \text{Eq. (i-1)}$$

616 where V_0 is a target cell volume, λ_{Adh}, λ_{P}, and λ_{V} are coefficient of cell-cell adhesion,
617 that of apical constriction, and that of the cell volume constraint, respectively. To derive a
618 potential energy in the simplest form, we assumed the geometry of single epithelial cells as
619 hexagonal prisms of base length r and height h. Since $S = 2\sqrt{3}rh$ and $P = 2\sqrt{3}r$, we
620 have

621 $$U_{\mathrm{Cell}} = 2\sqrt{3}rh\lambda_{\mathrm{Adh}} + 12\lambda_{\mathrm{P}} r^2 + \lambda_{\mathrm{V}} \left(V - V_0\right)^2, \qquad \text{Eq. (i-2)}$$

622 instead of Eq. (i-1). As shown in Figure 1D', the cell volume is almost constant even though
623 the cell shapes change with the inhibitor, i.e., $V = V_0$; therefore, we have $h = 2V_0 / \sqrt{3}r^2$
624 since $V = \sqrt{3}r^2 h / 2$. Substituting these into Eq. (i-2) leads to

625 $$\frac{r}{4} U_{\mathrm{Cell}} = V_0 \lambda_{\mathrm{Adh}} + 3\lambda_{\mathrm{P}} r^3. \qquad \text{Eq. (i-3)}$$

626 To remove prefactors provided by the assumption of hexagonal prism and make a
627 non-dimensional form, we substituted $r = r'\left(V_0/3\right)^{1/3}$ and $U_{\mathrm{Cell}} = U'_{\mathrm{Cell}} 4\left(1/3\right)^{-1/3} \lambda_{\mathrm{Adh}} V_0^{2/3}$ into
628 Eq. (i-3), and then derived

629 $$U'_{\mathrm{Cell}} = \frac{1}{r'} + \frac{\lambda_{\mathrm{P}}}{\lambda_{\mathrm{Adh}}} r'^2. \qquad \text{Eq. (i-4)}$$

630 To obtain the apical cell area proportional to the square of cell base length at minimum of the
631 potential energy, we calculated $r'_{\mathrm{eq}} = \left(r' \middle| \partial U'_{\mathrm{Cell}} / \partial r' = 0\right)$, and then obtained

632

633 $$r'^2_{\mathrm{eq}} \sim \lambda_{\mathrm{P}}^{-2/3}. \qquad \text{Eq. (i-5)}$$

634

635 Eq. (i-5) indicates that apical cell area/cell height becomes larger/shorter when the apical
636 constriction becomes weaker in the inhibitor (note $h = 2V_0 / \sqrt{3}r^2$), which is consistent with

our experimental results. Furthermore, this shows that the base length of cells r'_{eq} becomes larger in the inhibitor, meaning the tubule composed of the cells should expand by the inhibitors. Therefore, it is reasonable that mechanical force balance only within cells in the tubule determines the morphological change of tubule observed in our experiments.

(ii) Basic Formalization of the Vertex Dynamics Model

We employed a vertex dynamics model (VDM), a type of cell-oriented model, to represent multi-cellular dynamics in epithelial tissues [15,16,36–41]. In this model, a cell is geometrically regarded as a polygon/polyhedron, of which vertices are elementary points that constitute the cell shape, and a group of cells can be represented by a set of polygons/polyhedrons shared by neighboring cells [17,42–44]. In this study, we paid notice to apical junctions of the epididymal tubule on which a marker of tension generator pMRLC is only localized (Fig. 1A), and modeled the developing single-layered epithelial tube as a flexible multicellular membrane in 3D space according to earlier studies [45,46].

In the VDM, the dynamics of position of vertex *i*, $\mathbf{r}_i$, obey the equation of motion based on the principle of least potential energy *U* as follows:

$$\eta\left(\frac{d\mathbf{r}_i}{dt}-\langle\mathbf{v}_i\rangle\right)=-\nabla_i U\,, \qquad \text{Eq. (ii-1)}$$

where η is a viscosity coefficient, and $\langle\mathbf{v}_i\rangle$ is a local velocity of vertex *i*, defined as

$$\langle\mathbf{v}_i\rangle=\frac{\sum_{\alpha_i}^{n_{\alpha_i}} d\mathbf{r}_{\alpha_i}/dt}{n_{\alpha_i}}\,, \qquad \text{Eq. (ii-2)}$$

where α_i is an index for cells contacting to vertex *i*, n_{α_i} is a number of the cells contacting to vertex *i*, and $\mathbf{r}_{\alpha_i}$ is a centroid of cell α_i [38,47,48]. For a potential energy as a minimum expression to represent epididymal tubule cells, we defined as

$$U=\sum_{\alpha}\left\{\frac{\lambda_{\mathrm{A}}}{2}\left(A_\alpha-A_\alpha^{\mathrm{O}}\right)^2+\frac{\lambda_{\mathrm{P}}}{2}P_\alpha^2\right\}+\sum_i\frac{\lambda_{\mathrm{B}}}{2}\kappa_i^2A_i+\sum_j\left\{\gamma_j^{\mathrm{cst}}L_j-\gamma_j^{\mathrm{ext}}H(L^{\mathrm{O}}-L_j)\right\}, \qquad \text{Eq. (ii-3)}$$

according to earlier studies [16,36,49]. α, *i*, and *j* each denote an index of cells, that of vertices, and that of junctions/edges. The first term represents the cell elasticity; λ_{A} is its

coefficient, A_α is area of cell α, and A_α^{O} is a target area of cells. The second term represents isotropic actomyosin contractility at the periphery of apical junctions; λ_{P} is its coefficient and P_α is perimeter of the cell α. The third term represents bending energy of the flexible epithelial membrane embedded in 3D space; λ_{B} is its coefficient, κ_i is a discrete mean curvature defined at vertex *i* of triangular meshes [50], and A_i is summation of an area of triangular mesh fractions around vertex *i*, each explained one by one. For calculation of the discrete mean curvature at a vertex, let surface of the modeled epithelial membrane be a set of triangular meshes consisting of both the vertex of cells and the centroid of cells (Fig. S1A). Then, we defined the discrete mean curvature at vertex *i* as

$$\kappa_i = \frac{1}{2S_i}\left|\sum_{k\in V_i}\left(\cot\theta_{i,k}^1 + \cot\theta_{i,k}^2\right)\left(\mathbf{r}_i - \mathbf{r}_k\right)\right|, \qquad \text{Eq. (ii-4)}$$

where *k* is an index of the triangular elements included in the set of 1-ring neighbor vertices of the vertex *i*, V_i, S_i is total area of triangular meshes in V_i, $\theta_{i,k}^1$ and $\theta_{i,k}^2$ are each angle depicted in Figure S1A'. See [50] for more details. For calculation of A_i, let us consider triangles consisting a vertex and its 1-ring neighbor cell centroids illustrated in Figure S1A", and then sum the all triangles up around the vertex. In earlier studies, bending energy was defined as a summation of inner product of unit normal vectors to the surfaces between the adjacent cells [45,46]. This is valid when all mesh size is ideally equal [51,52]; therefore, we introduced the bending energy function based on the discrete curvature. The last term represents anisotropic junction constriction/extension; $\gamma_j^{\mathrm{cst/ext}}$ is its coefficient assigned to each edge, L_j is length of edge, L^{O} is a target edge length, and *H* is the Heaviside step function. For the simulation in Fig. 2F-F", 4, and S1, $\gamma_j^{\mathrm{cst/ext}}$=0. The details of this term are described later.

(iii) Normalized form of the model

By introducing a characteristic cell size A_0, the equations were transformed into nondimensionalized form to reduce the number of parameters as

$$\frac{d\mathbf{r}_i'}{dt'} - \left\langle \mathbf{v}_i' \right\rangle = -\nabla_i' U', \qquad \text{Eq. (iii-1)}$$

where $t' = t\lambda_{\mathrm{A}}A_0/\eta$, $\mathbf{r}_i' = \mathbf{r}_i/\sqrt{A_0}$, $\mathbf{r}_{\alpha_i}' = \mathbf{r}_{\alpha_i}/\sqrt{A_0}$, $\nabla' = \nabla\sqrt{A_0}$, $U' = U/\left(\lambda_{\mathrm{A}}A_0^2\right)$, and

$$U' = \sum_{\alpha}\left\{\frac{1}{2}\left(A'_{\alpha} - A'^{\mathrm{O}}_{\alpha}\right)^2 + \frac{\lambda'_{\mathrm{P}}}{2}P'^2_{\alpha}\right\} + \sum_{i}\frac{\lambda'_{\mathrm{B}}}{2}\kappa'^2_i A'_i + \sum_{j}\left\{\gamma'^{\mathrm{cst}}_j L'_j - \gamma'^{\mathrm{ext}}_j H(L^{\mathrm{O}} - L'_j)\right\},$$

Eq. (iii-2)

where $A'_{\alpha} = A_{\alpha}/A_0$, $A'^{\mathrm{O}}_{\alpha} = A^{\mathrm{O}}_{\alpha}/A_0$, $P'_{\alpha} = P_{\alpha}/\sqrt{A_0}$, $\kappa'_i = \kappa_i\sqrt{A_0}$, $A'_i = A_i/A_0$, $L'_j = L_j/\sqrt{A_0}$, $L^{\mathrm{O}} = L^{\mathrm{O}}/\sqrt{A_0}$, $\lambda'_{\mathrm{P}} = \lambda_{\mathrm{P}}/(\lambda_{\mathrm{A}}A_0)$, $\lambda'_{\mathrm{B}} = \lambda_{\mathrm{B}}/(\lambda_{\mathrm{A}}A_0^2)$, $\gamma'^{\mathrm{cst/ext}}_j = \gamma^{\mathrm{cst/ext}}_j/(\lambda_{\mathrm{A}}A_0^{-3/2})$. In addition, we introduced a normalized simulation time defined as $\tau' = t'/T^{\mathrm{cycle}}$, where T^{cycle} is an average cell cycle length, which will be explained. We used these variables and equations, Eq. (iii-1) and (iii-2), for the numerical simulations in this study.

(iv) Cell intercalation, Proliferation, and Simulation Conditions

As for the cell intercalation, we assumed that edge rearrangement occurred when the normalized length of edge became smaller than 0.05 and the edge length was set to be 0.1 after the edge rearrangement. See [44] for details of the edge rearrangement.

As for the cell proliferation, we introduced the average cell cycle length T^{cycle}, and set cell cycle length of each cell $T^{\mathrm{cycle}}_{\alpha}$ obey the normal distribution of which the mean is T^{cycle} and the standard deviation is 5% of the mean, i.e., $T^{\mathrm{cycle}}_{\alpha} \sim N(T^{\mathrm{cycle}}, 0.05T^{\mathrm{cycle}})$. Also, we introduced normalized cell cycle time of each cell as $\tau'^{\mathrm{cycle}}_{\alpha} = t'^{\mathrm{cycle}}_{\alpha}/T^{\mathrm{cycle}}_{\alpha}$, where $t'^{\mathrm{cycle}}_{\alpha}$ is nondimensionalized cell cycle time of cell α. $\tau'^{\mathrm{cycle}}_{\alpha}$ at t'=0 was assigned within 0 to 0.95 in uniform distribution. As the average cell cycle length in the epididymal tubule can be roughly estimated as 24 hours and cell volume tends to get increasing within the apical surface of epididymal tubule since 50-100 min before the cytokinesis, we simply modeled the cell dynamics during cell cycle as $A'^{\mathrm{target}}_{\alpha} = 1$ for $0 \le \tau'^{\mathrm{cycle}}_{\alpha} < 0.95$, $A'^{\mathrm{target}}_{\alpha} = 20\tau'^{\mathrm{cycle}}_{\alpha} - 18$ for $0.95 \le \tau'^{\mathrm{cycle}}_{\alpha} < 1$, and the cell divides with returning $A'^{\mathrm{target}}_{\alpha}$ of daughter cells to 1.The type of cell division orientation was set as follows – circumferential/longitudinal division: uniform distribution in a range of $\pm 0.05\pi$ from the circumferential/longitudinal axis of tube, and non-biased division: uniform distribution in all range of θ defined in the local coordinate at cell (Fig. 2C).

As initial condition for the simulation, we set that a virtual tube was composed of 14

cells along the circumferential direction based on our observation and of 30 cells along the longitudinal axis as for extensive numerical simulations. The cross-sectional center of the tube was set at y=0 and z=0 of global coordinate and the tube was put along the x axis. As boundary condition, the following energy was added to the original potential energy U' at tip cells of the tube:

$$\sum_{\alpha_{\text{tip}}} \lambda'_{\text{bnd}} \left(\sqrt{(r'^{y}_{\alpha_{\text{tip}}})^2 + (r'^{z}_{\alpha_{\text{tip}}})^2} - R'_0 \right)^2 , \qquad \text{Eq. (iv-1)}$$

where α_{tip} is an index for the tip cells of tube, λ'_{bnd} is its coefficient, R'_0 is a normalized mean radius of the tube to a characteristic cell length $\sqrt{A_0}$ in the initial setting, $r'^{y}_{\alpha_{\text{tip}}}$, and $r'^{z}_{\alpha_{\text{tip}}}$ each represent the relative position of center of cells α_{tip} on y and z axis to $\sqrt{A_0}$. This energy restricts displacement of the cells α_{tip} in radial direction of the tube, which imitates physical constraints by the vas deferens and the efferent ducts as boundary tissues of the epididymal tubule. We set $\lambda'_{\text{bnd}} = 0.1$ in the simulations.

(v) Mechano-responsive and Scheduled regimes

In the following, we explain the last two terms of Eq. (iii-2): the anisotropic edge constriction and extension after the cell intercalation. We here introduce a state variable assigned to each cell, $\Theta_\alpha = \{0,1,2\}$; $\Theta_\alpha = 0,1,2$ represent a naïve state (colored in white, Fig. 6B), edge-constriction state (red, Fig. 6B), and edge-extension state (blue, Fig. 6B), respectively. For all cells, $\Theta_\alpha = 0$, γ'^{cst}_j =0, and γ'^{ext}_j =0, unless otherwise noted. In our simulation, the following procedures were conducted for both 'mechano-responsive' and 'scheduled' regime. First, cells α' that might become a constricting cell were selected and let the state variable of the cell $\Theta_{\alpha'} = 1$; the way of selecting cells depends on each regime, i.e, the mechano-responsive or the scheduled regime. Second, one of the edges that orients to circumferential axis of the tube (the angle ϑ_j is within 70° – 90°) was selected among all edges composing the cells α', and index the edge j'. Then, state of cells including the edge j' turned to $\Theta_{\alpha'} = 1$. Third, the constriction of edge j' was performed according to a schedule as shown in Figure S4A; we set the edge kept constricting in a period τ'^{cst} via transition period τ'^{trns} from the starting point of edge constriction by an assumption with

752 phosphorylation process of pMRLC. The maximum value of $\gamma'^{\mathrm{cst}}_{j'}$ was set to be γ'^{cst}. $\Theta_{\alpha'}$
753 and $\gamma'^{\mathrm{cst}}_{j'}$ return to 0 at the end of edge constriction process. In this study, parameter
754 dependence of τ'^{cst} and that of γ'^{cst} were examined and determined (Fig. S4B), and we set
755 $\tau'^{\mathrm{trns}} = 0.02$. Finally, if the edge arrangement occurred during the process of edge
756 constriction ($\Theta_{\alpha'} = 1$), then the state of cells having the rearranged edge changes to $\Theta_{\alpha'} = 2$
757 and the edge becomes an extension mode, in which the rearranged edge converges to a
758 constant target length; $\gamma'^{\mathrm{cst}}_{j'} = 0$, $\gamma'^{\mathrm{ext}}_{j'} = 0.01$, and $L^{\mathrm{O}} = 0.1$. We set the period of edge
759 extension as $\tau'^{\mathrm{ext}} = 0.02$. $\Theta_{\alpha'}$ and $\gamma'^{\mathrm{ext}}_{j'}$ return to 0 after the process of edge extension. Our
760 implementation for the edge extension process is based on an earlier report that the junction
761 after the cell intercalation grows due to local polarized force driven by medial actomyosin
762 contraction [49].
763 As for the way of selecting the cells α' in the first step described above, we adopted
764 the two: mechano-responsive and scheduled regime. On the mechano-responsive regime, we
765 supposed that the epididymal tubule cells could receive mechanical stress provided by
766 adjacent cells, and a stress tensor in cells α in the local cell coordinate system *O'* was
767 defined as
768
769 $$\sigma_\alpha = \left(A'_\alpha - A'^{\mathrm{O}}_\alpha\right)\mathbf{I} + \sum_{j_\alpha}\left(\lambda'_{\mathrm{P}} + \gamma'^{\mathrm{cst}}_{j_\alpha} - \gamma'^{\mathrm{ext}}_{j_\alpha}\right)\frac{\mathbf{a}_{j_\alpha} \otimes \mathbf{a}_{j_\alpha}}{L'_{j_\alpha} A'_\alpha}, \qquad \text{Eq. (v-1)}$$
770
771 where $\mathbf{I}$ is a unit tensor, j_α is an index of edges composing the cell α, $\mathbf{a}$ is a vector
772 representing the relative position of two vertices composing the edge j_α [53–55].
773 Denoting a diagonal element of the tensor σ_α corresponding to the longitudinal axis of the
774 tube and that to the circumferential axis as $\sigma^{\mathrm{long}}_\alpha$ and $\sigma^{\mathrm{circ}}_\alpha$, we then defined the cell tension
775 anisotropy as
776
777 $$\rho_\alpha = \sigma^{\mathrm{long}}_\alpha - \sigma^{\mathrm{circ}}_\alpha. \qquad \text{Eq. (v-2)}$$
778
779 Note that the cell tension anisotropy ρ_α is a time-dependent variable. In the
780 mechano-responsive regime, the cells were assigned as α' when ρ_α was over a threshold

ρ^*, of which parameter dependency for the resulting tube morphology was examined (Fig. S4B).

On the scheduled regime, the cells α' were randomly selected but timing of the selection was predetermined according to the schedule shown in Figure 6C; Figure 6C shows the fraction of cells having constricting edges to all tube cells in the mechano-responsive regime (n=10, gray), and its mean (black). In our simulation, we used the following logistic function (blue) by fitting the mean curve with the least-squared method:

$$f(\tau') = k_1\left(1+\exp\left[-k_2(\tau'-k_3)\right]\right)^{-1} \qquad \text{Eq. (v-3)}$$

with $k_1 = 0.1$, $k_2 = 0.01$, and $k_3 = 0.17$.

(vi) Morphological and Mechanical Quantities in Simulation

We used the following morphological quantities in the simulation; [1] tube length, i.e., longitudinal linear length between distal edges of tube, [2] tube diameter, i.e., mean diameter of circumferentially-averaged diameter through the centerline of tube, and [3] curvedness, i.e., averaged curvature of the vertices throughout the tube defined as $\sum_i \kappa'_i A'_i \Big/ \sum_i A'_i$.

For the cell tension anisotropy ρ_α, refer to the Eq. (v-2). For the tube tension anisotropy in Figure 2F, the stress tensor in the tube was defined as

$$\sigma_{\text{tube}} = \left[\sum_\alpha \left(A'_\alpha - A'^{\text{O}}_\alpha\right) A'_\alpha \mathbf{I} + \sum_j \left(\lambda'_{\text{P}} + \gamma'^{\text{cst}}_j - \gamma'^{\text{ext}}_j\right) \frac{\mathbf{a}_j \otimes \mathbf{a}_j}{L'_j}\right] \Big/ \sum_\alpha A'_\alpha, \qquad \text{Eq. (vi-1)}$$

according to earlier studies [53–55], and using its diagonal element $\sigma^{\text{long}}_{\text{tube}}$ and $\sigma^{\text{circ}}_{\text{tube}}$, we introduced

$$\rho_{\text{tube}} = \sigma^{\text{long}}_{\text{tube}} - \sigma^{\text{circ}}_{\text{tube}} \qquad \text{Eq. (vi-2)}$$

as the tube tension anisotropy. $\sigma^{\text{long}}_{\text{tube}}$ and $\sigma^{\text{circ}}_{\text{tube}}$ each correspond to the tube longitudinal tension and the tube circumferential tension appeared in Figure S1.

(vii) Determination of Parameter Values (Fig. S1 and Fig. S4)

Parameter values used in this study were (i) $\lambda'_{\text{P}}=10^{-2}$, $\lambda'_{\text{B}}=10^{0.75}$, (ii) $T^{\text{cycle}}=10^{3.75}$, (iii)

811 $\rho^* = 0.1$, $\gamma'^{\mathrm{cst}} = 1$, and $\tau'^{\mathrm{cst}} = 0.167$ unless otherwise noted. As for (i), we determined the
812 values, at which there were less variations at t'=1000 from the initial configuration (Fig.
813 S1B and S1B'). Note that no proliferation was implemented for this analysis. As for (ii), we
814 examined the parameter dependence of cell proliferation rate $1/T^{\mathrm{cycle}}$ to the morphological
815 and the mechanical quantities at $\tau' = 1$ (Fig. S1C). The results show that the cell division
816 orientation less affected to the tube shape (length and diameter) in faster cell proliferation
817 rate. In addition, smooth surface of tube was not maintained if the cell proliferation rate was
818 larger than $10^{-3.5}$ (see curvedness in Fig. S1C). This is because the cell proliferation rate is
819 faster than relaxation time of tube in the dynamics. We determined as $T^{\mathrm{cycle}}=10^{3.75}$. As for
820 (iii), we examined the parameter dependence of ρ^*, γ'^{cst}, and τ'^{cst} to the tube shape and
821 its variance at $\tau' = 1$ (Fig. S4B). We first determined $\rho^* = 0.1$ because the coefficient of
822 variation (CV) became larger at $\rho^* = 0.08$ and there were less differences of the mean
823 values to the variation of γ'^{cst} at $\rho^* = 0.125$. Then, we determined $\gamma'^{\mathrm{cst}} = 1$ because this
824 point is at a boundary for both the mean and the CV. Finally, as for τ'^{cst}, we arbitrarily set
825 the value because there were less differences in any values.
826
827
828 **(IV) Others**
829 **(i) Statistical Hypothesis Testing**
830 Exact information of the statistical tests, sample sizes, test statistics, and *P*-values were
831 described in the Supplemental Information. Statistical hypothesis testing was performed
832 according to [56]. *P*-values of less than 0.05 were considered to be statistically significant in
833 two-tailed tests, and were classified as 4 categories; * (P<0.05), ** (P<0.01), *** (P<0.001),
834 and n.s. (not significant, i.e., $P \geq 0.05$).
835
836 **(ii) Replicates and Sample Number**
837 All replicates in this study are biological replicates. The *n* in the figure legends indicates the
838 number of samples used for each analysis as described below.
839 Figure 1B′: *n* indicates the number of epididymides collected from 3 pregnant mice.
840 Figure 1D′: *n* indicates the number of cells randomly chosen from 3 epididymides collected
841 from a pregnant mouse.
842 Figure 2D and E: *n* indicates the number of cells sampled from 6 epididymides collected

843 from a pregnant mouse.
844 Figure 3C-F′: *n* indicates the number of apical edges sampled from 8 epididymides collected
845 from 2 pregnant mice.
846 Figure 3H and H′: *n* indicates the number of epididymides collected from 3 pregnant mice.
847 Figure J′ and J′′: *n* indicates the number of cells randomly chosen from 3 epididymides
848 collected from a pregnant mouse.
849 Figure 5E: *n* indicates the number of a group of cells sampled from 4 epididymides each
850 collected from 4 pregnant mice.
851 Figure 7D-D′′: *n* indicates the number of cells randomly chosen from 10 epididymides
852 collected from 3 pregnant mice.
853 Figure 7E′ and E′′: *n* indicates the number of pregnant mice.
854
855 **(iii) Graph**
856 Except for boxplot, we used mean as representative values, and error bars represent standard
857 deviation. Boxplots were drawn using R (GNU project).
858
859 **(iv) Software**
860 For digital image processing, we used MATLAB (MathWorks) and Image J (National
861 Institute of Health). For graphics, we used MATLAB (MathWorks), R (GNU project),
862 Gnuplot (Free Software), and Paraview (Kitware). For statistical analysis, we used MATLAB
863 (MathWorks) and R (GNU project).
864

865 Additional files

866 Additional files include full information of statistical hypothesis testing, and supplementary
867 five figures.
868
869

870 Author Contributions

871 T.H. performed experiments and simulations, and analyzed all data; T.H. and T.A. wrote the
872 manuscript.
873
874

875 Acknowledgements

This work was supported by the Platform Project for Supporting in Drug Discovery and Life Science Research (Platform for Dynamic Approaches to Living System) from the MEXT and the AMED, and by the JSPS KAKENHI grant 15K18541. We would like to thank T. Furukawa of Osaka Univ. for kindly providing the Pax2-Cre mice.

Competing Interests

The authors declare that no competing interests exist.

885 # References

886 [1] Guillot C, Lecuit T. Mechanics of epithelial tissue homeostasis and morphogenesis.
887 Science 2013;340:1185–9. doi:10.1126/science.1235249.
888 [2] Mammoto T, Mammoto A, Ingber DE. Mechanobiology and Developmental Control.
889 Annu Rev Cell Dev Biol 2013;29:27–61.
890 doi:10.1146/annurev-cellbio-101512-122340.
891 [3] Eisenhoffer GT, Rosenblatt J. Bringing balance by force: Live cell extrusion controls
892 epithelial cell numbers. Trends Cell Biol 2013;23:185–92.
893 doi:10.1016/j.tcb.2012.11.006.
894 [4] Hufnagel L, Teleman AA, Rouault H, Cohen SM, Shraiman BI. On the mechanism of
895 wing size determination in fly development. Proc Natl Acad Sci U S A
896 2007;104:3835–40. doi:10.1073/pnas.0607134104.
897 [5] Shraiman BI. Mechanical feedback as a possible regulator of tissue growth. Proc Natl
898 Acad Sci U S A 2005;102:3318–23. doi:10.1073/pnas.0404782102.
899 [6] Karner CM, Chirumamilla R, Aoki S, Igarashi P, Wallingford JB, Carroll TJ. Wnt9b
900 signaling regulates planar cell polarity and kidney tubule morphogenesis. Nat Genet
901 2009;41:793–9. doi:10.1038/ng.400.
902 [7] Hirashima T. Pattern Formation of an Epithelial Tubule by Mechanical Instability
903 during Epididymal Development. Cell Rep 2014;9:866–73.
904 doi:10.1016/j.celrep.2014.09.041.
905 [8] Andrew DJ, Ewald AJ. Morphogenesis of epithelial tubes: Insights into tube formation,
906 elongation, and elaboration. Dev Biol 2010;341:34–55.
907 doi:10.1016/j.ydbio.2009.09.024.
908 [9] Joseph A, Yao H, Hinton BT. Development and morphogenesis of the
909 Wolffian/epididymal duct, more twists and turns. Dev Biol 2009;325:6–14.
910 doi:10.1016/j.ydbio.2008.10.012.
911 [10] Watanabe T, Hosoya H, Yonemura S. Regulation of Myosin II Dynamics by
912 Phosphorylation and Dephosphorylation of Its Light Chain in Epithelial Cells. Mol
913 Biol Cell 2007;18:605–16. doi:10.1091/mbc.E06-07-0590.
914 [11] Kovács M, Tóth J, Hetényi C, Málnási-Csizmadia A, Seller JR. Mechanism of
915 blebbistatin inhibition of myosin II. J Biol Chem 2004;279:35557–63.
916 doi:10.1074/jbc.M405319200.
917 [12] Peterson LJ, Rajfur Z, Maddox AS, Freel CD, Chen Y, Edlund M, et al. Simultaneous

918 stretching and contraction of stress fibers in vivo. Mol Biol Cell 2004;15:3497–508.
919 doi:10.1091/mbc.E03-09-0696.
920 [13] Tang N, Marshall WF, McMahon M, Metzger RJ, Martin GR. Control of mitotic
921 spindle angle by the RAS-regulated ERK1/2 pathway determines lung tube shape.
922 Science (80-) 2011;333:342–5. doi:10.1126/science.1204831.
923 [14] Fischer E, Legue E, Doyen A, Nato F, Nicolas J-F, Torres V, et al. Defective planar
924 cell polarity in polycystic kidney disease. Nat Genet 2006;38:21–3.
925 doi:10.1038/ng1701.
926 [15] Fletcher AG, Osterfield M, Baker RE, Shvartsman SY. Vertex models of epithelial
927 morphogenesis. Biophys J 2014;106:2291–304. doi:10.1016/j.bpj.2013.11.4498.
928 [16] Rauzi M, Verant P, Lecuit T, Lenne P-F. Nature and anisotropy of cortical forces
929 orienting Drosophila tissue morphogenesis. Nat Cell Biol 2008;10:1401–10.
930 doi:10.1038/ncb1798.
931 [17] Nagai T, Honda H. A dynamic cell model for the formation of epithelial tissues. Philos
932 Mag Part B 2001;81:699–719. doi:10.1080/13642810108205772.
933 [18] Walck-Shannon E, Hardin J. Cell intercalation from top to bottom. Nat Rev Mol Cell
934 Biol 2014;15:34–48. doi:10.1038/nrm3723.
935 [19] Hirashima T, Adachi T. Procedures for the Quantification of Whole-Tissue
936 Immunofluorescence Images Obtained at Single-Cell Resolution during Murine
937 Tubular Organ Development. PLoS One 2015;10:e0135343.
938 doi:10.1371/journal.pone.0135343.
939 [20] Stewart MP, Helenius J, Toyoda Y, Ramanathan SP, Muller DJ, Hyman A a.
940 Hydrostatic pressure and the actomyosin cortex drive mitotic cell rounding. Nature
941 2011;469:226–30. doi:10.1038/nature09642.
942 [21] Abe T, Kiyonari H, Shioi G, Inoue KI, Nakao K, Aizawa S, et al. Establishment of
943 conditional reporter mouse lines at ROSA26 locus for live cell imaging. Genesis
944 2011;49:579–90. doi:10.1002/dvg.20753.
945 [22] Ohyama T, Groves AK. Generation of Pax2-Cre Mice by Modification of a Pax2
946 Bacterial Artificial Chromosome. Genesis 2004;38:195–9. doi:10.1002/gene.20017.
947 [23] Blanchard GB, Kabla AJ, Schultz NL, Butler LC, Sanson B, Gorfinkiel N, et al. Tissue
948 tectonics: morphogenetic strain rates, cell shape change and intercalation. Nat Methods
949 2009;6:458–64. doi:10.1038/nmeth.1327.
950 [24] Savin T, Kurpios NA, Shyer AE, Florescu P, Liang H, Mahadevan L, et al. On the
951 growth and form of the gut. Nature 2011;476:57–62. doi:10.1038/nature10277.

952 [25] Dong B, Hannezo E, Hayashi S. Balance between Apical Membrane Growth and
953 Luminal Matrix Resistance Determines Epithelial Tubule Shape. Cell Rep 2014.
954 doi:10.1016/j.celrep.2014.03.066.
955 [26] Beloussov L V. Morphomechanics of Development. Springer; 2015.
956 doi:10.1007/978-3-319-13990-6.
957 [27] Sasai Y. Cytosystems dynamics in self-organization of tissue architecture. Nature
958 2013;493:318–26. doi:10.1038/nature11859.
959 [28] Nishimura T, Honda H, Takeichi M. Planar cell polarity links axes of spatial dynamics
960 in neural-tube closure. Cell 2012;149:1084–97. doi:10.1016/j.cell.2012.04.021.
961 [29] Bosveld F, Bonnet I, Guirao B, Tlili S, Wang Z, Petitalot A, et al. Mechanical Control
962 of Morphogenesis by Fat/Dachsous/Four-Jointed Planar Cell Polarity Pathway.
963 Science (80-) 2012;336:724–7. doi:10.1126/science.1221071.
964 [30] Xu B, Washington AM, Domeniconi RF, Ferreira Souza AC, Lu X, Sutherland A, et al.
965 Protein tyrosine kinase 7 is essential for tubular morphogenesis of the Wolffian duct.
966 Dev Biol 2016;412:219–233.
967 [31] Yokomizo T, Yamada-Inagawa T, Yzaguirre AD, Chen MJ, Speck NA, Dzierzak E.
968 Whole-mount three-dimensional imaging of internally localized immunostained cells
969 within mouse embryos. Nat Protoc 2012;7:421–31. doi:Doi 10.1038/Nprot.2011.441.
970 [32] Susaki EA, Tainaka K, Perrin D, Kishino F, Tawara T, Watanabe TM, et al.
971 Whole-brain imaging with single-cell resolution using chemical cocktails and
972 computational analysis. Cell 2014;157:726–39. doi:10.1016/j.cell.2014.03.042.
973 [33] Kapur JN, Sahoo PK, Wong AKC. A new method for gray-level picture thresholding
974 using the entropy of the histogram. Comput Vision, Graph Image Process 1985;29:140.
975 doi:10.1016/S0734-189X(85)90156-2.
976 [34] Kerschnitzki M, Kollmannsberger P, Burghammer M, Duda GN, Weinkamer R,
977 Wagermaier W, et al. Architecture of the osteocyte network correlates with bone
978 material quality. J Bone Miner Res 2013;28:1837–45. doi:10.1002/jbmr.1927.
979 [35] Hannezo E, Prost J, Joanny J-F. Theory of epithelial sheet morphology in three
980 dimensions. Proc Natl Acad Sci 2014;111:27–32. doi:10.1073/pnas.1312076111.
981 [36] Farhadifar R, Röper J-C, Aigouy B, Eaton S, Jülicher F. The influence of cell
982 mechanics, cell-cell interactions, and proliferation on epithelial packing. Curr Biol
983 2007;17:2095–104. doi:10.1016/j.cub.2007.11.049.
984 [37] Bielmeier C, Alt S, Weichselberger V, La Fortezza M, Harz H, J??licher F, et al.
985 Interface Contractility between Differently Fated Cells Drives Cell Elimination and

986 Cyst Formation. Curr Biol 2016;26:563–74. doi:10.1016/j.cub.2015.12.063.
987 [38] Mao Y, Tournier AL, Hoppe A, Kester L, Thompson BJ, Tapon N. Differential
988 proliferation rates generate patterns of mechanical tension that orient tissue growth.
989 EMBO J 2013;32:2790–803. doi:10.1038/emboj.2013.197.
990 [39] Honda H, Motosugi N, Nagai T, Tanemura M, Hiiragi T. Computer simulation of
991 emerging asymmetry in the mouse blastocyst. Development 2008;135:1407–14.
992 doi:10.1242/dev.014555.
993 [40] Trichas G, Smith AM, White N, Wilkins V, Watanabe T, Moore A, et al.
994 Multi-cellular rosettes in the mouse visceral endoderm facilitate the ordered migration
995 of anterior visceral endoderm cells. PLoS Biol 2012;10.
996 doi:10.1371/journal.pbio.1001256.
997 [41] Aegerter-Wilmsen T, Heimlicher MB, Smith AC, de Reuille PB, Smith RS, Aegerter
998 CM, et al. Integrating force-sensing and signaling pathways in a model for the
999 regulation of wing imaginal disc size. J Cell Sci 2012;125:e1–e1.
1000 doi:10.1242/jcs.120758.
1001 [42] Honda H, Eguchi G. How much does the cell boundary contract in a monolayered cell
1002 sheet? J Theor Biol 1980;84:575–88. doi:10.1016/S0022-5193(80)80021-X.
1003 [43] Honda H, Tanemura M, Nagai T. A three-dimensional vertex dynamics cell model of
1004 space-filling polyhedra simulating cell behavior in a cell aggregate. J Theor Biol
1005 2004;226:439–53. doi:10.1016/j.jtbi.2003.10.001.
1006 [44] Fletcher AG, Osborne JM, Maini PK, Gavaghan DJ. Implementing vertex dynamics
1007 models of cell populations in biology within a consistent computational framework.
1008 Prog Biophys Mol Biol 2013;113:299–326. doi:10.1016/j.pbiomolbio.2013.09.003.
1009 [45] Osterfield M, Du X, Schüpbach T, Wieschaus E, Shvartsman SY. Three-Dimensional
1010 Epithelial Morphogenesis in the Developing Drosophila Egg. Dev Cell 2013;24:400–
1011 10. doi:10.1016/j.devcel.2013.01.017.
1012 [46] Du X, Osterfield M, Shvartsman SY. Computational analysis of three-dimensional
1013 epithelial morphogenesis using vertex models. Phys Biol 2014;11:66007.
1014 doi:10.1088/1478-3975/11/6/066007.
1015 [47] Ishimoto Y, Morishita Y. Bubbly vertex dynamics: A dynamical and geometrical
1016 model for epithelial tissues with curved cell shapes. Phys Rev E - Stat Nonlinear, Soft
1017 Matter Phys 2014;90. doi:10.1103/PhysRevE.90.052711.
1018 [48] Okuda S, Inoue Y, Eiraku M, Adachi T, Sasai Y. Vertex dynamics simulations of
1019 viscosity-dependent deformation during tissue morphogenesis. Biomech Model

Mechanobiol 2014;14:413–25. doi:10.1007/s10237-014-0613-5.

[49] Collinet C, Rauzi M, Lenne P, Lecuit T. Local and tissue-scale forces drive oriented junction growth during tissue extension. Nat Cell Biol 2015;17:1247–58. doi:10.1038/ncb3226.

[50] Meyer M, Desbrun M, Schr P, Barr AH. Discrete Differential-Geometry Operators for Triangulated 2-Manifolds. Vis Math III 2003:113–34. doi:10.1016/j.cagd.2007.07.005.

[51] Kantor Y, Nelson DR. Crumpling transition in polymerized membranes. Phys Rev Lett 1987;58:2774–7. doi:10.1103/PhysRevLett.58.2774.

[52] Seung HS, Nelson DR. Defects in flexible membranes with crystalline order. Phys Rev A 1988;38:1005–18. doi:10.1103/PhysRevA.38.1005.

[53] Batchelor GK. The stress system in a suspension of force-free particles. J Fluid Mech 1970;41:545–70. doi:10.1017/S0022112070000745.

[54] Ishihara S, Sugimura K. Bayesian inference of force dynamics during morphogenesis. J Theor Biol 2012;313:201–11. doi:Doi 10.1016/J.Jtbi.2012.08.017.

[55] Sugimura K, Ishihara S. The mechanical anisotropy in a tissue promotes ordering in hexagonal cell packing. Development 2013;140:4091–101. doi:10.1242/dev.094060.

[56] Zar JH. Biostatistical Analysis, 5th Edition. 2014.

1039 # Figure Legends

1040

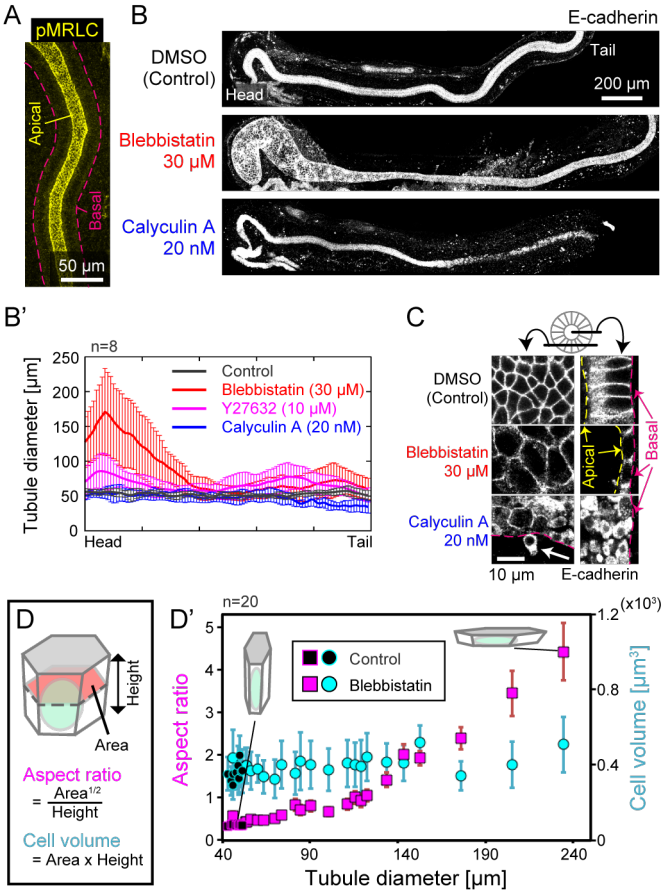

1041

1042

1043 **Figure 1 Actomyosin-mediated apical constriction is required for the maintenance of**
1044 **the tubule radial size.**

1045 (A) Maximum intensity projection (MIP) of immunofluorescence images for the pMRLC in
1046 epididymis at E16.5. Magenta dotted lines represent the basal of epididymal tubule. Scale
1047 bar: 50 µm. (B and B´) Morphological change of tubules in the inhibitor assays. (B) MIP of
1048 immunofluorescence images for the E-cadherin. The head region of epididymis to the tail
1049 from left to right. Scale bar: 200 µm. (B´) The tubule diameter along the tubule. *n*=8. (C-C´´)
1050 Morphological change of tubule cells in the inhibitor assays. (C) Immunofluorescence images
1051 for the E-cadherin at sections of the tubule. Yellow/magenta lines represent apical/basal of
1052 the cells. Scale bar: 10 µm. (D) Schematic for the cell morphology quantities; the aspect ratio
1053 is defined as the squared cell area over the cell height and the cell volume is defined as the
1054 cell area times the cell height. (D´) The cell morphology quantities versus the tubule diameter
1055 in the control and blebbistatin treatment. *n*=20.

1056

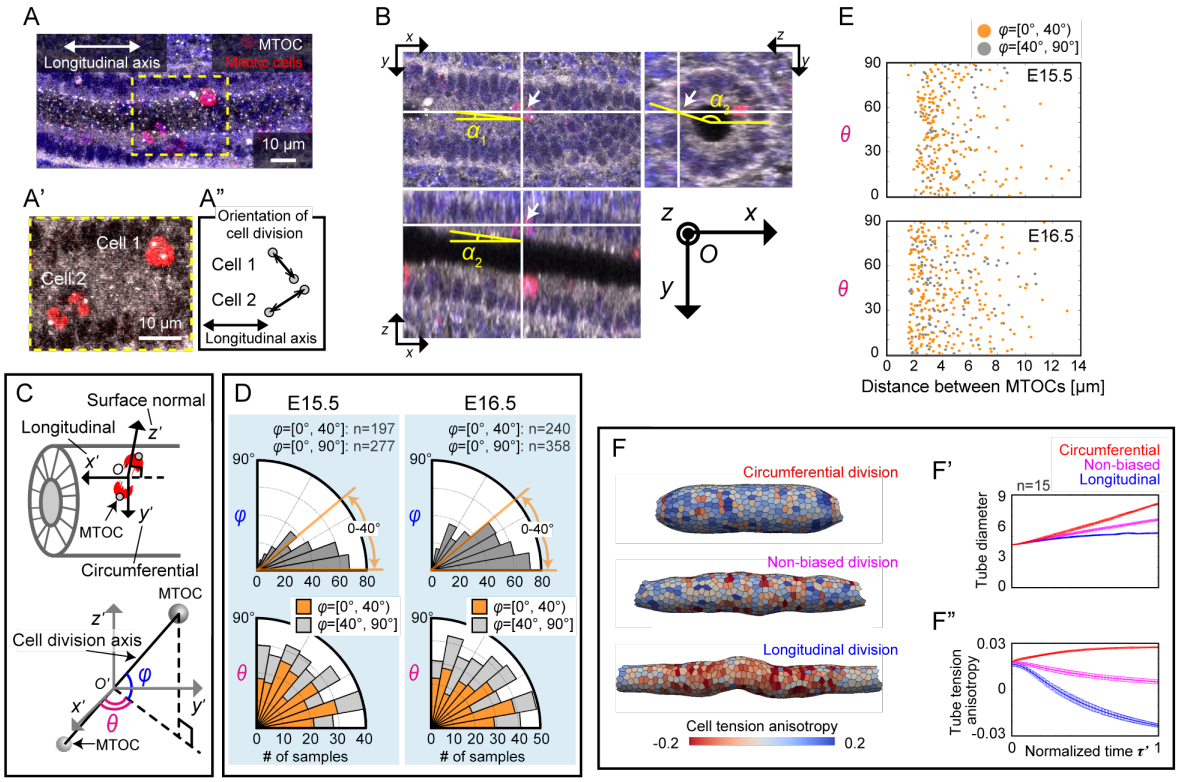

Figure 2 Cell division orientation determines the mechanical stress and tubule radial size.

(A) MIP of immunostained images for the pHH3 (mitotic cells, red) and γ-tubulin (MTOCs, white). (A′ and A′′) Magnified view of the dotted square in (A), displaying the two cells divide in different orientations. Scale bars: 10 μm. (B) Measurement of cell division orientation in the tubule. Arrows indicate the center position of the mitotic cell. Using the three angles α_1, α_2, and α_3, the observation coordinate O is transformed into the local coordinate O' in Fig. 2C. (C) Illustration of the local coordinates. (D) The angle distributions for the cell division orientation. Colors in the θ distribution represent samples, of which φ ranges from 0-40 degrees (orange) and from 40-90 degrees (gray). (E) Scatter plot for the distance between MTOCs and the angle θ. The sample number is the same as in (D). (F-F′′) Model simulations in different cell division orientations. (F) The vertex dynamics model simulation of proliferating tubes. The cell division orientation determines the mechanical stress in the cells and tubule radial size. The color represents the cell tension anisotropy. (F′ and F′′) Time course of morphological and mechanical quantities along the normalized simulation time τ'. See the Materials and Methods (III-v) and (III-vi) for those quantities and Materials and Methods (III-iii) for the definition of τ'. n=15.

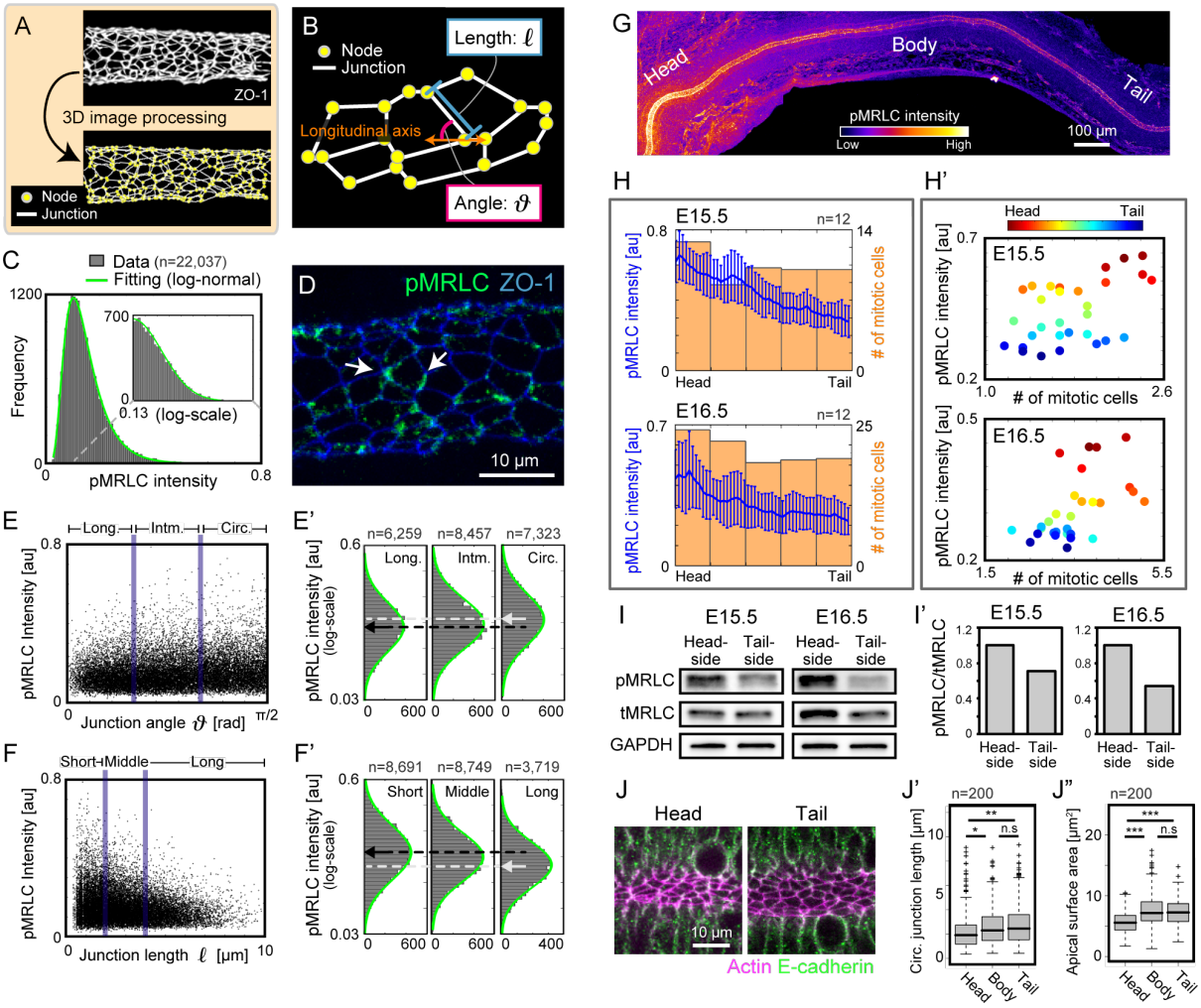

Figure 3 Polarized apical constriction is coupled to cell division.

(A) Digital processing from immunofluorescence images for the ZO-1 detects nodes and junctions of apical surfaces. (B) Illustration of the junction angle ϑ and length ℓ. ϑ measures the angle from the longitudinal axis of tubules. (C) Histogram of pMRLC intensity (gray) fitted with a log-normal distribution (green). The small window displays the tail of distribution, showing the well-fitting. n=22,037. (D) MIP of co-immunostained images of pMRLC (green) and ZO-1 (blue). Arrows indicate pMRLC localization at circumferential junctions. Scale bar: 10 μm. (E-F′) Relationship between the pMRLC intensity and the junction angle/length. The log-scale histograms are shown in three divided groups. Black arrows represent the mean intensity in the longitudinal/short group and white arrows represent that in the circumferential/long group. (G) MIP of pMRLC immunostaining at the whole-tissue scale. Scale bar: 100 μm. (H) Spatial profile of pMRLC intensity (blue) and the number of mitotic cells (orange) along the tubule. n=12. (H′) The pMRLC intensity versus the mitotic cell number. The color indicates position of data in the tubule. (I and I′) Myosin activity quantification by immunoblotting. (J-J′′) Apical junction morphology visualized by

1093 staining for the F-actin and E-cadherin. *n*=200. Scale bar: 10 μm.

1094

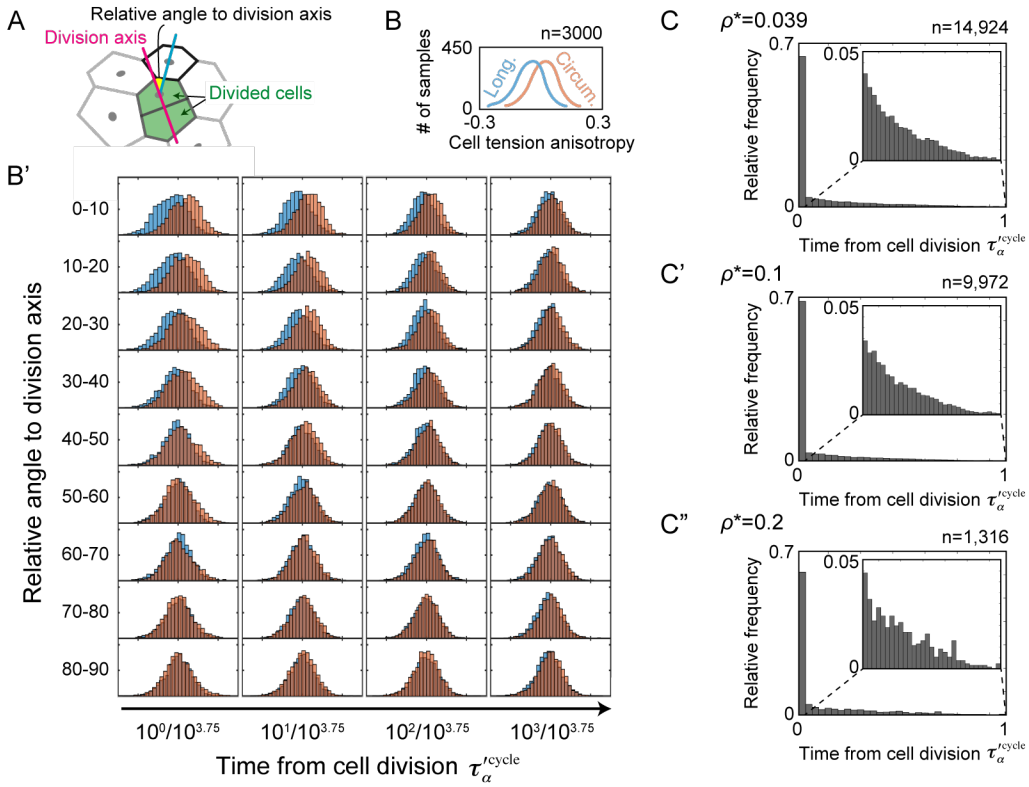

Figure 4 Computational analysis of cell stress influenced by cell division in tubes. (A) The schematics for glossary. The cell tension anisotropy was calculated in cells neighboring to the divided cells. (B and B′) Histograms of cell tension anisotropy against the cell divisions. (B) The explanatory illustration for the histograms. Red indicates the case of circumferential cell division and blue indicates the case of longitudinal cell division. (B′) Histograms of the cell tension anisotropy in various cases of the relative angle to the cell division axis (vertical) and in those of the elapsed time of neighbors' cell division $\tau_\alpha'^{cycle}$ (horizontal). (C-C′′) Histograms of the elapsed time after the cell division $\tau_\alpha'^{cycle}$ when the cell tension anisotropy is over various thresholds (ρ^*=0.039, 0.1, and 0.2) in neighboring cells on the circumferential axis. The tail of histograms is magnified in the small windows.

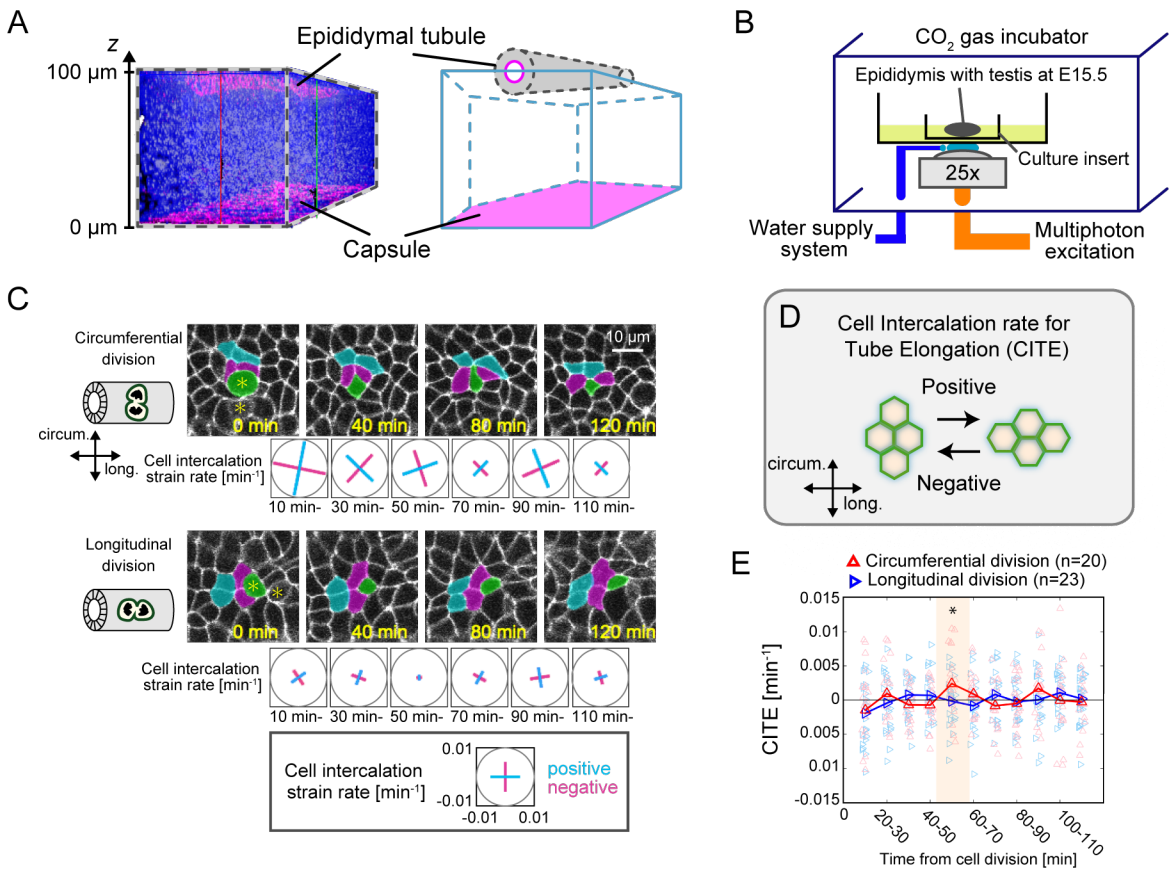

Figure 5 Live imaging revealed that the oriented cell division occurs following to the circumferential cell division.

(A) The dimensions of epididymis. The rendering image from the immunofluorescence for the ZO-1 (magenta) (left) and its schematics (right). (B) The schematics for the incubator-integrated multiphoton excitation microscopy system. (C) Snapshots from live imaging data in the case of the circumferential and longitudinal cell divisions. Time origin is at the timing of cytokinesis completion. Asterisks represent daughters of divided cell, one of which is colored artificially in green. Some cells are also colored for easy visualization. The scale and sign for cell intercalation strain rate is shown in the bottom. Scale bar: 10 µm. (D) Schematics for the CITE. (E) The time series data for the case of circumferential cell division (red, n=20) and that of the longitudinal division (blue, n=23). Time zone in which the mean value is not statistically zero is highlighted.

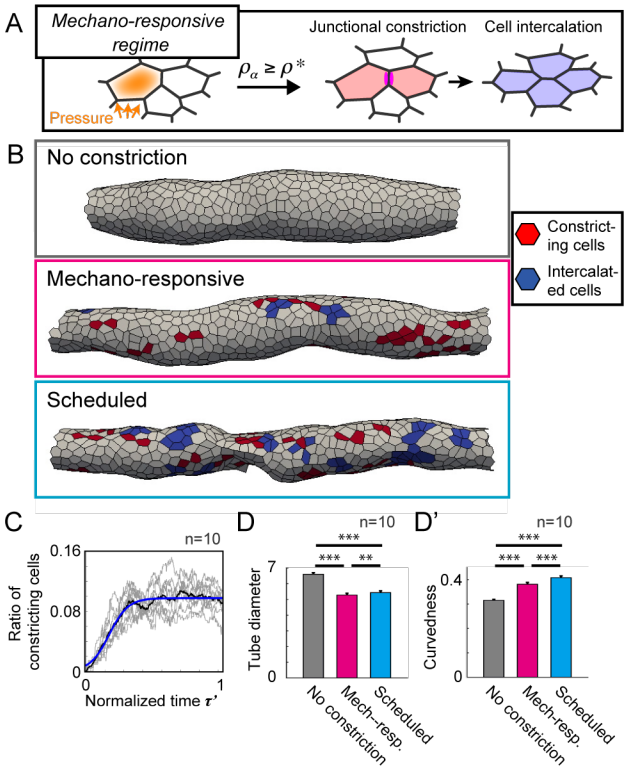

Figure 6 Model simulations suggest that the mechano-responsive cell behavior explains the maintenance of tubule radial size.

(A) Schematics for the mechano-responsive regime. In this regime, the circumferential junction constriction starts when the cell tension anisotropy becomes larger than the threshold ρ^* due to the pressure from circumferentially-neighboring cells. (B) Generated tubes in different regimes: no constriction, mechano-responsive, and scheduled. Red color in the tubes represents cells constricting the circumferential junction and blue represents cells that have completed the cell intercalation. (C) The ratio of constricting cells to the total cells over the normalized simulation time τ' in the mechano-responsive regime: data in each simulation (gray), the mean value (black) and fitting with the logistic function (blue). n=10. (D and D′) Resulting morphological quantities of tubes, the tube diameter and the tube curvedness, in different regimes. See the Materials and Methods (III-vi) for the definition of those morphological quantities. n=10.

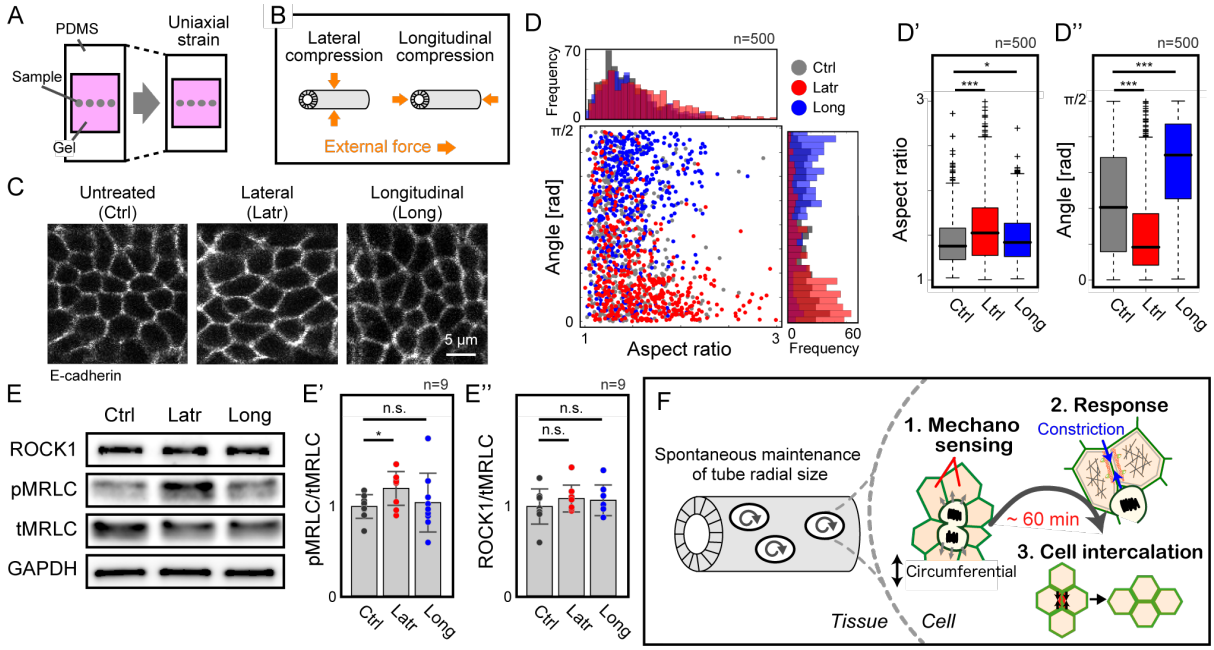

Figure 7 Mechanical perturbation assays uncovered the polarized mechano-response system for the maintenance of tubule radial size.

(A and B) Schematics for the uniaxial compression assays. (C) Morphology of the tubule cells following the mechanical treatments. The cell shape was recognized by immunofluorescence for the E-cadherin. Scale bar: 5 μm. (D-D´´) The aspect ratio and the major axis angle for each treatment: control (gray), lateral compression (red), and longitudinal compression (blue). The data are shown as scatter plot and histogram in (D) and as boxplot in (D´ and D´´). *n*=500. (E-E´´) Immunoblotting and quantification of myosin activity and ROCK1 for the mechanical treatments. The tubule cells activate myosin as a cellular response to lateral compression. (E´ and E´´) The data are normalized to the mean value in the control. *n*=9. (F) Model for the maintenance of tubule radial size.

Additional files (Supplemental Information)

Anisotropic Cellular Mechanoresponse for Radial Size Maintenance of Developing Epithelial Tubes

Tsuyoshi Hirashima and Taiji Adachi

This file includes:

Statistical Hypothesis Testing
Supplementary Figures S1 to S5
Still images and captions for Movies 1 to 3

Statistical Hypothesis Testing

The statistical tests, sample sizes, test statistics, and *P*-values were described below. *P*-values of less than 0.05 were considered to be statistically significant in two-tailed tests, and were classified as 4 categories; * ($P<0.05$), ** ($P<0.01$), *** ($P<0.001$), and n.s. (not significant, i.e., $P \geq 0.05$).

- Figure 2D, φ at E15.5

Note: The range of data was transformed to 0-360º for circular distributions.

H_0: The population of φ at E15.5 is uniformly distributed around the circle.

H_A: The population of φ at E15.5 is not uniformly distributed around the circle.

The Rayleigh test. n=277, Test statistic: Z=35.51, P<0.001; Reject H_0.

- Figure 2D, θ at E15.5

Note: The range of data was transformed to 0-360º for circular distributions.

H_0: The population of θ at E15.5 is uniformly distributed around the circle.

H_A: The population of θ at E15.5 is not uniformly distributed around the circle.

The Rayleigh test. n=197 (0-40º), Test statistic: Z=0.40, P=0.67; Do not reject H_0.

The Rayleigh test. n=277 (0-90º), Test statistic: Z=0.25, P=0.78; Do not reject H_0.

- Figure 2D, φ at E16.5

Note: The range of data was transformed to 0-360º for circular distributions.

H_0: The population of φ at E16.5 is uniformly distributed around the circle.

H_A: The population of φ at E16.5 is not uniformly distributed around the circle.

The Rayleigh test. n=358, Test statistic: Z=27.32, P<0.001; Reject H_0.

- Figure 2D, θ at E16.5

Note: The range of data was transformed to 0-360º for circular distributions.

H_0: The population of θ at E16.5 is uniformly distributed around the circle.

H_A: The population of θ at E16.5 is not uniformly distributed around the circle.

The Rayleigh test. n=240 (0-40º), Test statistic: Z=1.95, P=0.14; Do not reject H_0.

The Rayleigh test. n=358 (0-90º), Test statistic: Z=0.57, P=0.56; Do not reject H_0.

- Figure 3E’

Note: The data were transformed on logarithmic scale.

H_0: The mean intensities of pMRLC among the three groups of junction angle are all equal.

H_A: The mean intensities of pMRLC among the three groups of junction angle are not all equal.

One-way analysis of variance. n=6,259 (Longitudinal), n=8,457 (Intermediate), n=7,323 (Circumferential), Test statistic: F=165.47, P<0.001; Reject H_0.

Multiple comparisons using the Tukey-Kramer Test with unequal sample sizes: P<0.001 (Long. vs. Intm.), P<0.001 (Long. vs. Circ.), and P<0.001 (Intm. vs. Circ.).

- Figure 3F'

Note: The data were transformed on logarithmic scale.

H_0: The mean intensities of pMRLC among the three groups of junction length are all equal.

H_A: The mean intensities of pMRLC among the three groups of junction length are not all equal.

One-way analysis of variance. n=8,691 (Short), n=8,749 (Middle), n=3,719 (Long), Test statistic: F=306.65, P<0.001; Reject H_0.

Multiple comparisons using the Tukey-Kramer test with unequal sample sizes: P<0.001 (Short. vs. Middle), P<0.001 (Short vs. Long), and P<0.001 (Middle vs. Long).

- Figure 3J'

H_0: The circumferential edge length is the same in all three regions of epididymal tubule.

H_A: The circumferential edge length is not the same in all three regions of epididymal tubule.

The Kruskal-Wallis test, n=200 for all groups, Test statistic: H=14.84, P<0.001; Reject H_0.

Steel-Dwass multiple comparisons: P=0.016 (Head vs. Body), P=0.001 (Head vs. Tail), P=0.61 (Body vs. Tail).

- Figure 3J"

H_0: The apical surface area is the same in all three regions of epididymal tubule.

H_A: The apical surface area is not the same in all three regions of epididymal tubule.

The Kruskal-Wallis test, n=200 for all groups, Test statistic: H=89.58, P<0.001; Reject H_0.

Steel-Dwass multiple comparisons: P<0.001 (Head vs. Body), P<0.001 (Head vs. Tail), P=0.71 (Body vs. Tail).

- Figure 5C

H_0: The mean value of CITE in a certain time zone from the cell division is equal to zero.

H_A: The mean value of CITE in a certain time zone from the cell division is not equal to zero.

t test, n=20 in the case of circumferential cell division and n=23 in that of longitudinal one,

Test statistic: absolute value of t: $|t|$

[Circ., 10-20 min]: $|t|$=0.97, P=0.34; Do not reject H_0

[Circ., 20-30 min]: $|t|$=1.01, P=0.32; Do not reject H_0

[Circ., 30-40 min]: $|t|$=1.12, P=0.29; Do not reject H_0

[Circ., 40-50 min]: $|t|$=1.06, P=0.30; Do not reject H_0

[Circ., 50-60 min]: $|t|$=2.37, P=0.03; Reject H_0

[Circ., 60-70 min]: $|t|$=1.50, P=0.15; Do not reject H_0

[Circ., 70-80 min]: $|t|$=1.09, P=0.29; Do not reject H_0

[Circ., 80-90 min]: $|t|$=0.54, P=0.59; Do not reject H_0

[Circ., 90-100 min]: $|t|$=1.75, P=0.10; Do not reject H_0

[Circ., 100-110 min]: $|t|$=0.04, P=0.97; Do not reject H_0

[Circ., 110-120 min]: $|t|$=0.35, P=0.73; Do not reject H_0

[Long., 10-20 min]: $|t|$=2.02, P=0.06; Do not reject H_0

[Long., 20-30 min]: $|t|$=0.51, P=0.61; Do not reject H_0

[Long., 30-40 min]: $|t|$=1.05, P=0.30; Do not reject H_0

[Long., 40-50 min]: $|t|$=0.98, P=0.34; Do not reject H_0

[Long., 50-60 min]: $|t|$=0.21, P=0.83; Do not reject H_0

[Long., 60-70 min]: $|t|$=1.03, P=0.31; Do not reject H_0

[Long., 70-80 min]: $|t|$=1.08, P=0.29; Do not reject H_0

[Long., 80-90 min]: $|t|$=0.31, P=0.76; Do not reject H_0

[Long., 90-100 min]: $|t|$=0.03, P=0.97; Do not reject H_0

[Long., 100-110 min]: $|t|$=1.75, P=0.09; Do not reject H_0

[Long., 110-120 min]: $|t|$=0.24, P=0.81; Do not reject H_0

- Figure 6D

H_0: The mean values of tube diameter among the three groups of regime are all equal.

H_A: The mean values of tube diameter among the three groups of regime are not all equal.

One-way analysis of variance, n=10 for all groups, F=791.10, P<0.001; Reject H_0.

Tukey multiple comparisons: P<0.001 (No constriction vs. Mech-resp.), P<0.001 (No constriction vs. Scheduled), and P=0.002 (Mech-resp vs. Scheduled).

- Figure 6D'

H_0: The mean values of curvedness among the three groups of regime are all equal.
H_A: The mean values of curvedness among the three groups of regime are not all equal.
One-way analysis of variance, n=10 for all groups, F=575.25, P<0.001; Reject H_0.
Tukey multiple comparisons: P<0.001 (No constriction vs. Mech-resp.), P<0.001 (No constriction vs. Scheduled), and P<0.001 (Mech-resp vs. Scheduled).

- Figure 7D'

H_0: The aspect ratio of cells is the same in all three treatments of compression assay.
H_A: The aspect ratio of cells is not the same in all three treatments of compression assay.
The Kruskal-Wallis test, n=500 for all groups, Test statistic: H=42.10, P<0.001; Reject H_0.
Steel multiple comparisons: P<0.001 (Control vs. Lateral), P=0.043 (Control vs. Longitudinal).

- Figure 7D"

H_0: The angle of cells is the same in all three treatments of compression assay.
H_A: The angle of cells is not the same in all three treatments of compression assay.
The Kruskal-Wallis test, n=500 for all groups, Test statistic: H=366.04, P<0.001; Reject H_0.
Steel multiple comparisons: P<0.001 (Control vs. Lateral), P<0.001 (Control vs. Longitudinal).

- Figure 7E'

H_0: The ratio of pMRLC to tMRLC is the same in all three treatments of compression assay.
H_A: The ratio of pMRLC to tMRLC is not the same in all three treatments of compression assay.
The Friedman test, n=9 for all groups, Test statistic: Q=6, P=0.049; Reject H_0.
Steel multiple comparisons: P=0.039 (Control vs. Lateral), P=1.82 (Control vs. Longitudinal).

- Figure 7E'

H_0: The ratio of ROCK1 to tMRLC is the same in all three treatments of compression assay.
H_A: The ratio of ROCK1 to tMRLC is not the same in all three treatments of compression assay.
The Friedman test, n=9 for all groups, Test statistic: Q=1.56, P=0.46; Do not reject H_0.

1306 Steel multiple comparisons: P=0.50 (Control vs. Lateral), P=0.60 (Control vs. Longitudinal).

1307

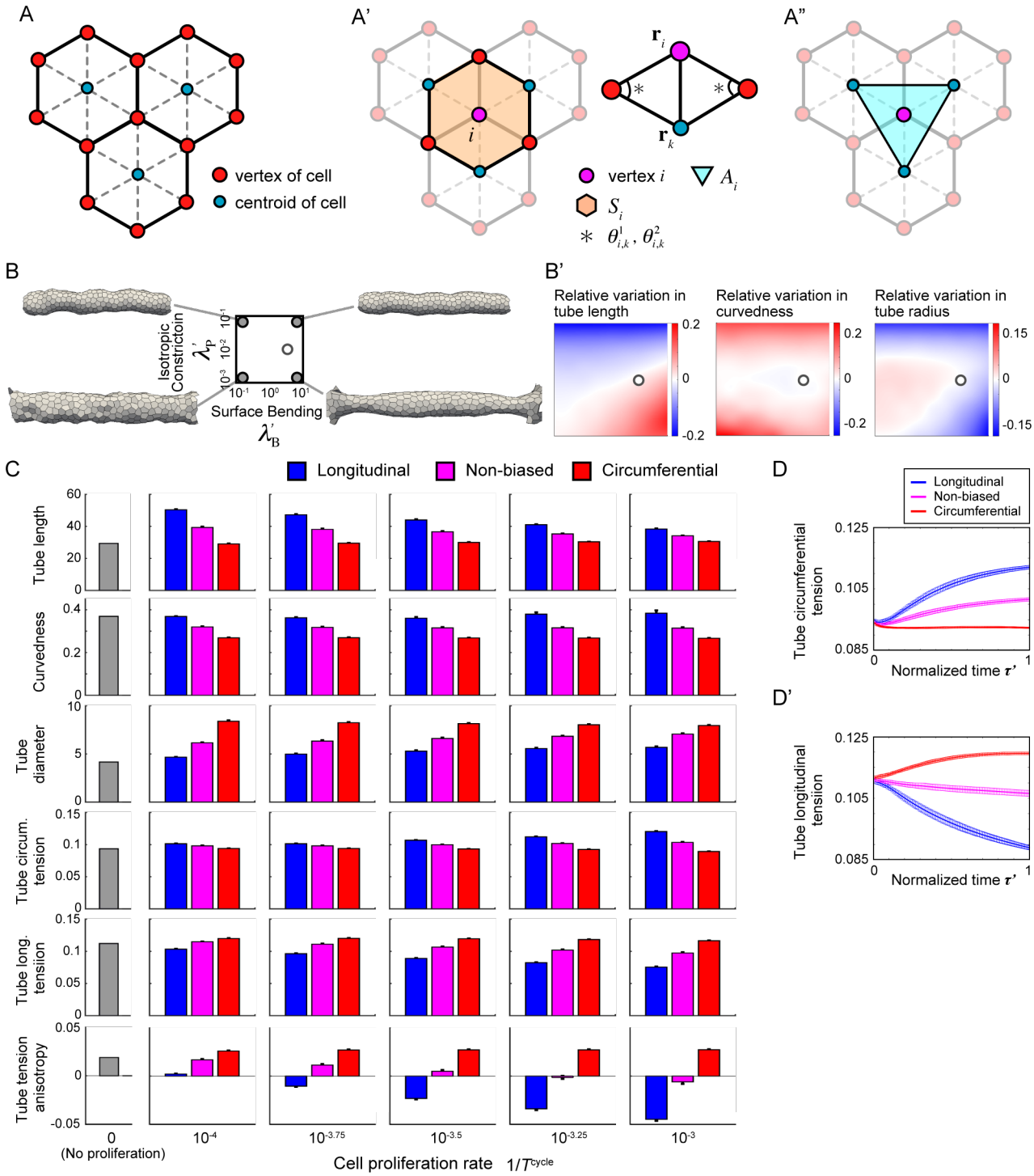

Figure S1 Preparation for the simulation without anisotropic junction constriction, corresponding to the Figure 2

(A-A") Schematics for the explanation of discrete curvature in the vertex model. See the Materials and Methods (III-ii) for the notations. (B and B') Diagram of generated tube morphology for parameters λ'_B and λ'_P, and relative variation of morphological quantities in the absence of cell proliferation. Tubes are visualized in the four corners of parameter space (filled circles). Open circles represent parameter values used in this study. The axes labels are

shown in B. (C) Parameter dependence of morphological and mechanical quantities for cell division orientation and cell proliferation rate. Color represents the type of cell division orientation. (D and D') Time course of tube circumferential tension and that of tube longitudinal tension. See the Materials and Methods (III-vi) for the definition of tube circumferential/longitudinal tension.

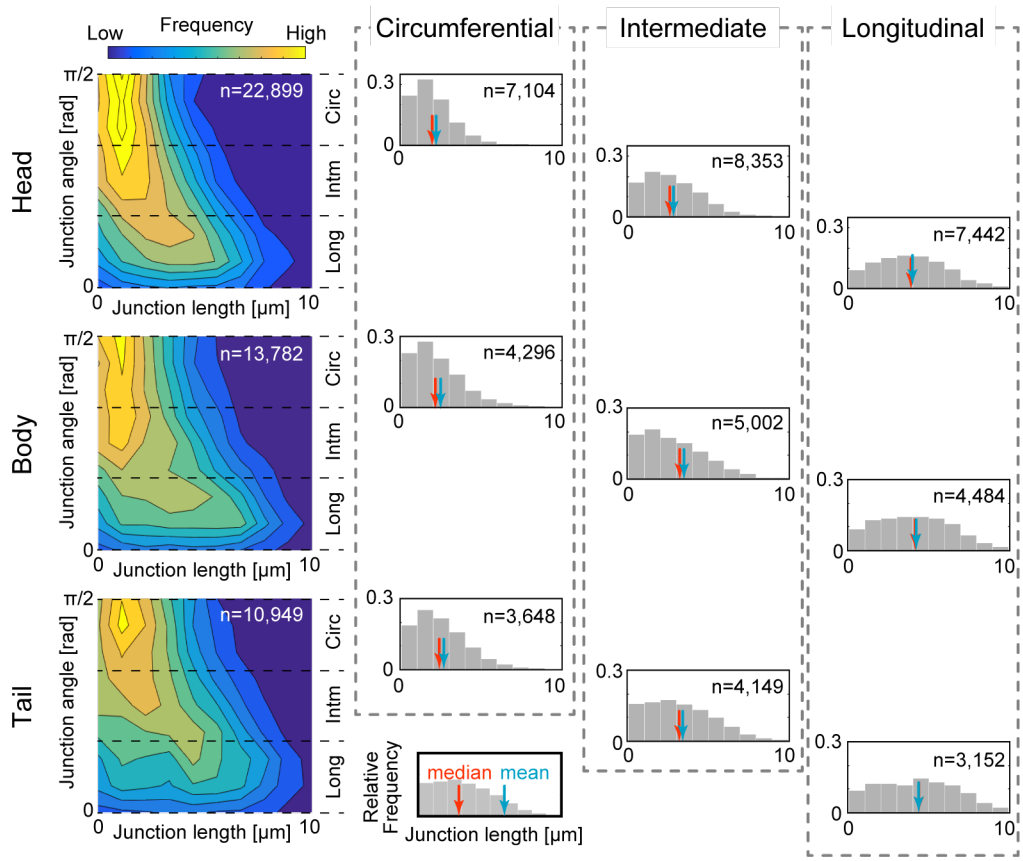

Figure S2 Apical junction length and angle, corresponding to the Figure 3

Frequency map on junction length ℓ and angle θ (left). Relative frequency in each region of epididymal tubule (Head, Body, and Tail) and angle category (Longitudinal, Intermediate, and Circumferential) is shown as histograms (right). The red/blue arrow indicates median/mean. The axis label of histograms is represented in the bottom. The circumferential junction length is shorter than the longitudinal junction length in any regions. In addition, the circumferential junction length in the head region is shorter than that in the tail region.

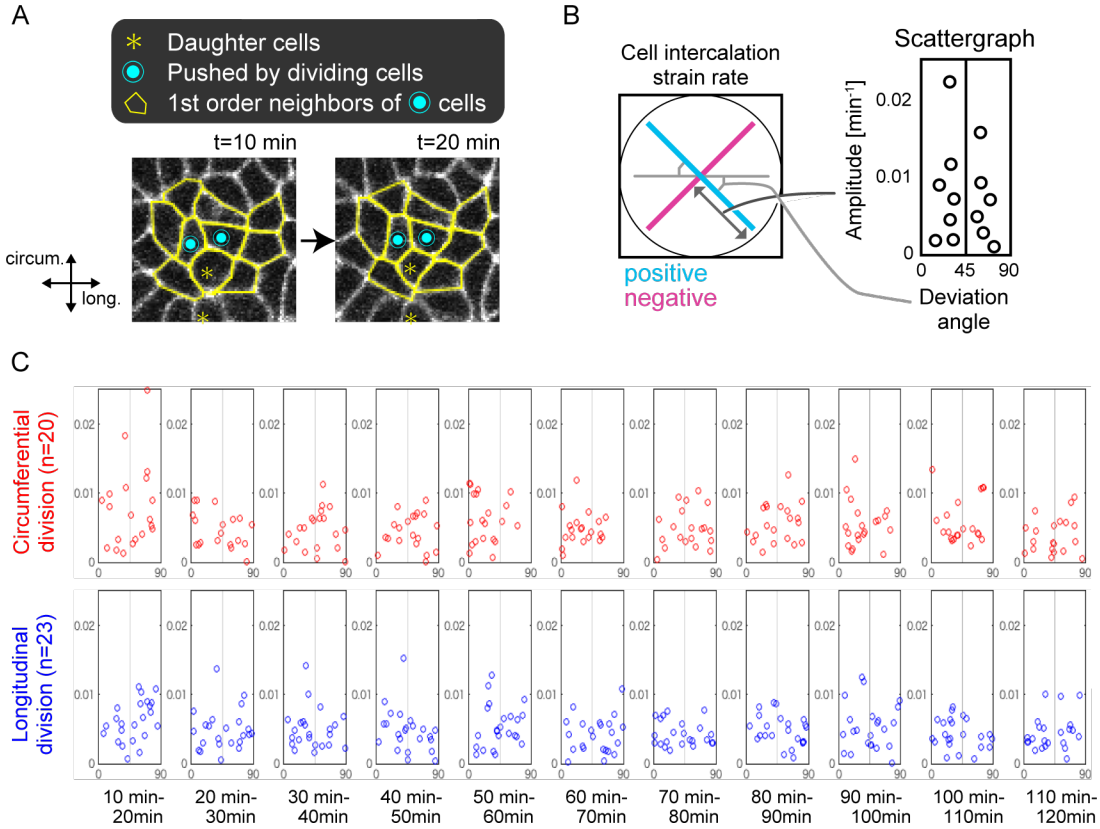

Figure S3 Measurement of cell intercalation strain rate from the live imaging data, corresponding to the Figure 5

(A) Illustration for target cells to calculate the cell intercalation strain rate. See the Materials and Methods (II-viii) for the details. (B) Graph representations for the cell intercalation strain rate. Orthogonal lines in the left graph represent principal strain rate. The amplitude and angle deviation of the positive principal strain rate (blue) in the left are expressed in the right angle-amplitude graph. (C) Time course of the cell intercalation strain rate as in the form of angle-amplitude graph for each type of cell division orientation: circumferential cell division and longitudinal one.

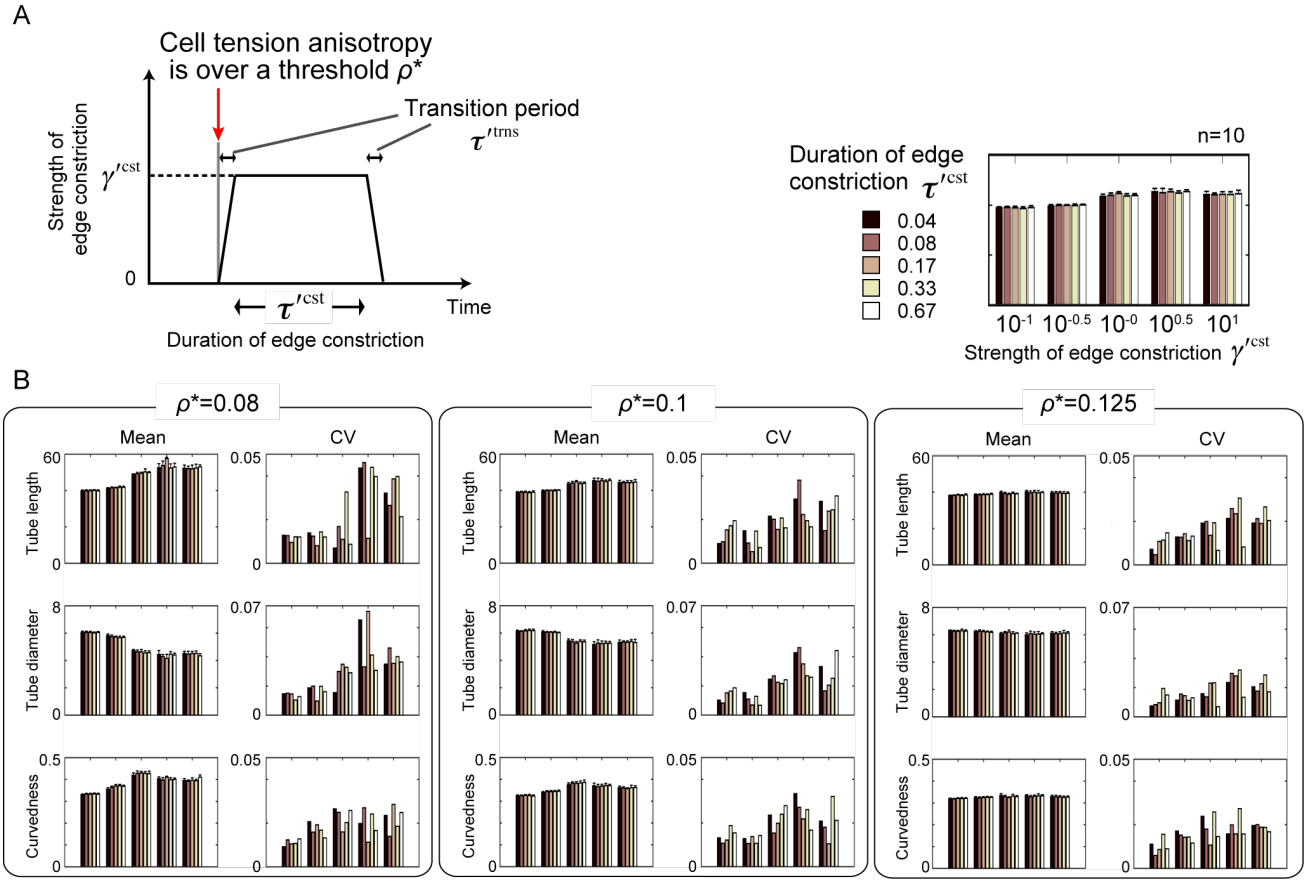

Figure S4 Preparation for the simulations in the mechano-responsive regime, corresponding to the Figure 6

(A) Schematics for the model. See the Materials and Methods (III-v) for the details. (B) Parameter dependence of tube morphology. The referenced graph is shown in the upper right. CV: coefficient of variance. See the Materials and Methods (III-vii) for determining the parameter values.

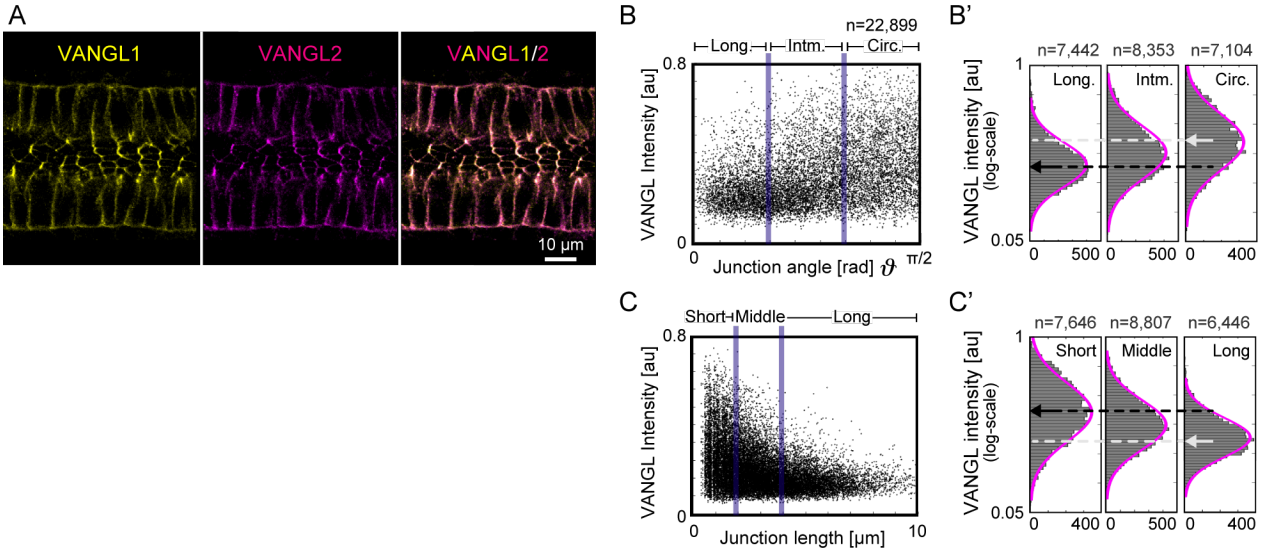

Figure S5 Spatial distribution of polarity proteins Van like protein (VANGL) 1 and 2, corresponding to the Discussion

(A) Immunofluorescence for VANGL1 and VANGL2 demonstrates that their co-localizations are on circumferential junctions of epididymal tubule. (B-C') Relation of junction angle v.s. the fluorescence intensity, and that of junction length v.s. the intensity as with the form of Fig. 3E-F'. These graphs indicate the VANGL localization on the apical junctions of tubule shows significant polarization.

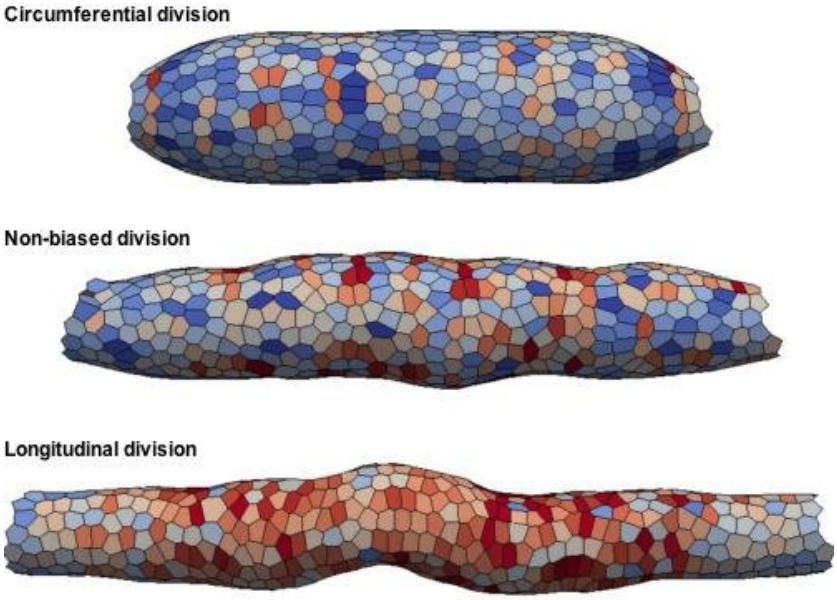

Movie 1 Model Simulation in Different Cell Division Orientation

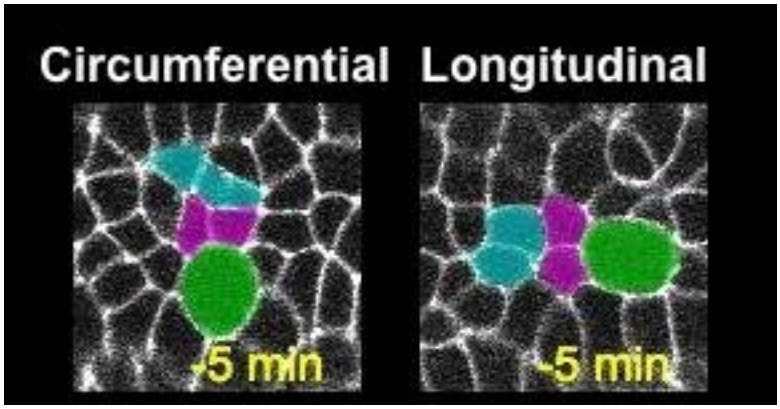

Movie 2 Live Imaging for Multicellular Behaviors against Cell Division

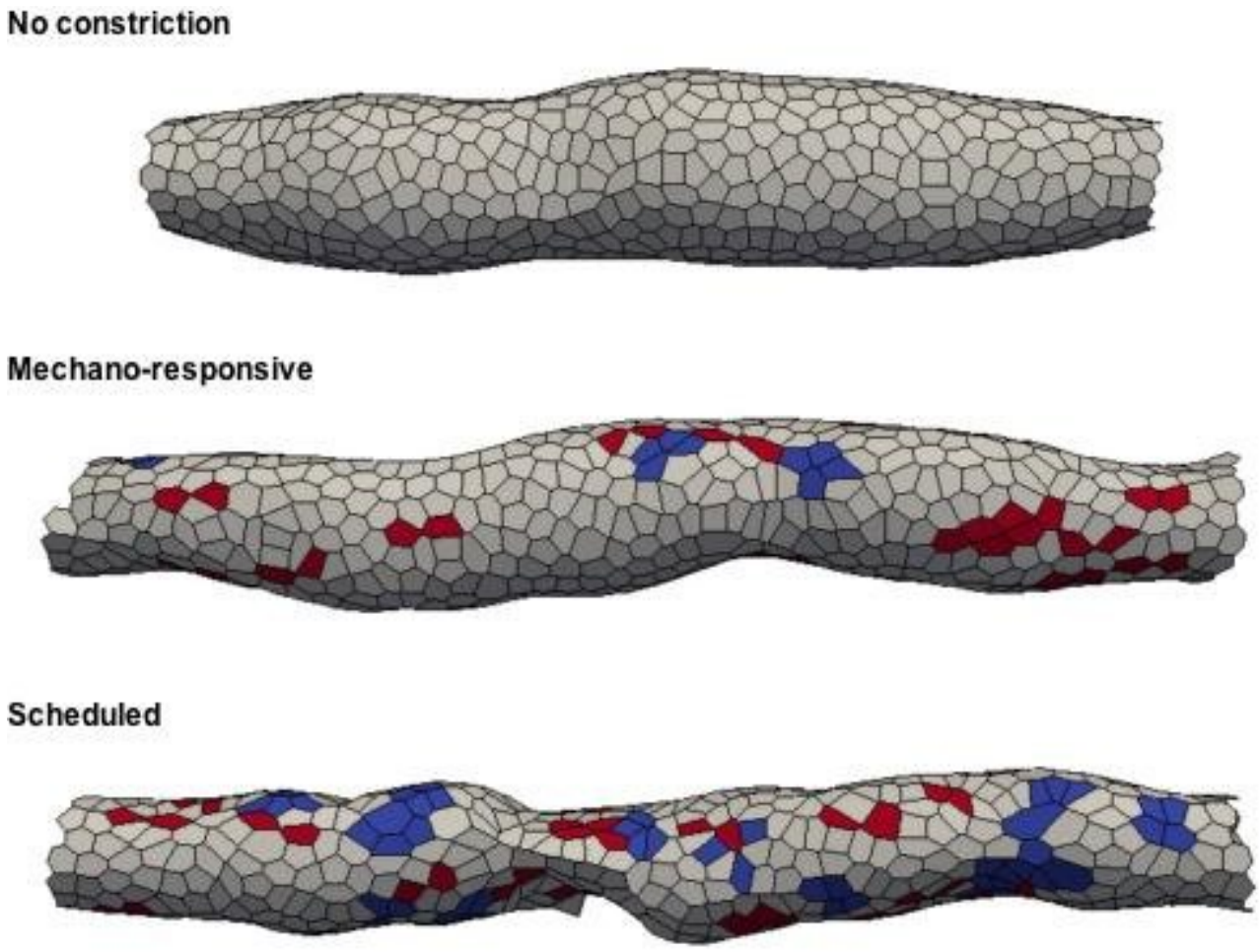

Movie 3 Model Simulation in Different Regimes

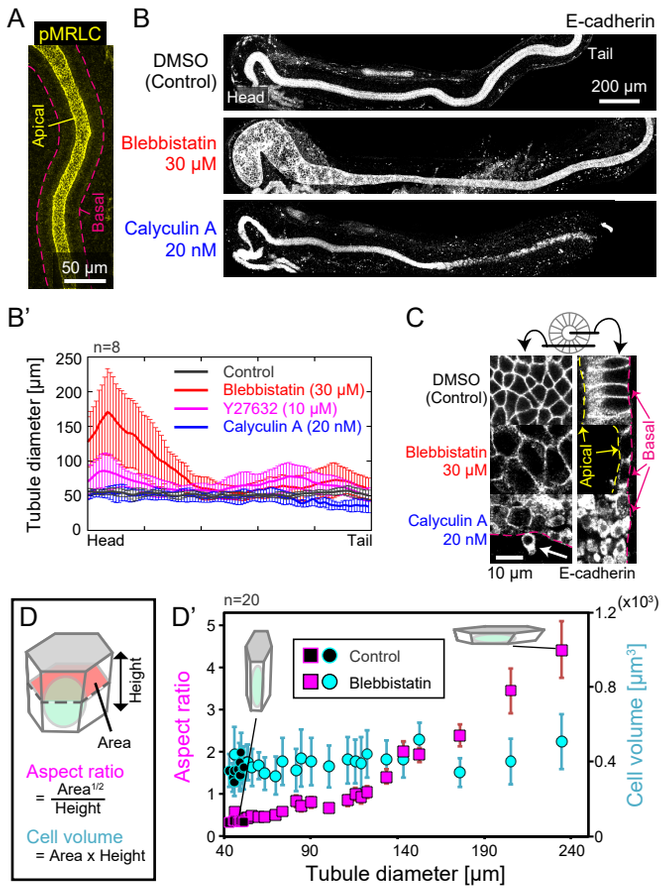
A
pMRLC
Apical
Basal
50 µm
B
E-cadherin
DMSO
(Control)
Head
Tail
200 µm
Blebbistatin
30 µM
Calyculin A
20 nM
B'
n=8
Tubule diameter [µm]
Control
Blebbistatin (30 µM)
Y27632 (10 µM)
Calyculin A (20 nM)
Head
Tail
C
DMSO
(Control)
Blebbistatin
30 µM
Calyculin A
20 nM
Apical
Basal
10 µm
E-cadherin
D
Height
Area
Aspect ratio
= Area^1/2 / Height
Cell volume
= Area x Height
D'
n=20
Control
Blebbistatin
Aspect ratio
Cell volume [µm³]
(x10³)
Tubule diameter [µm]

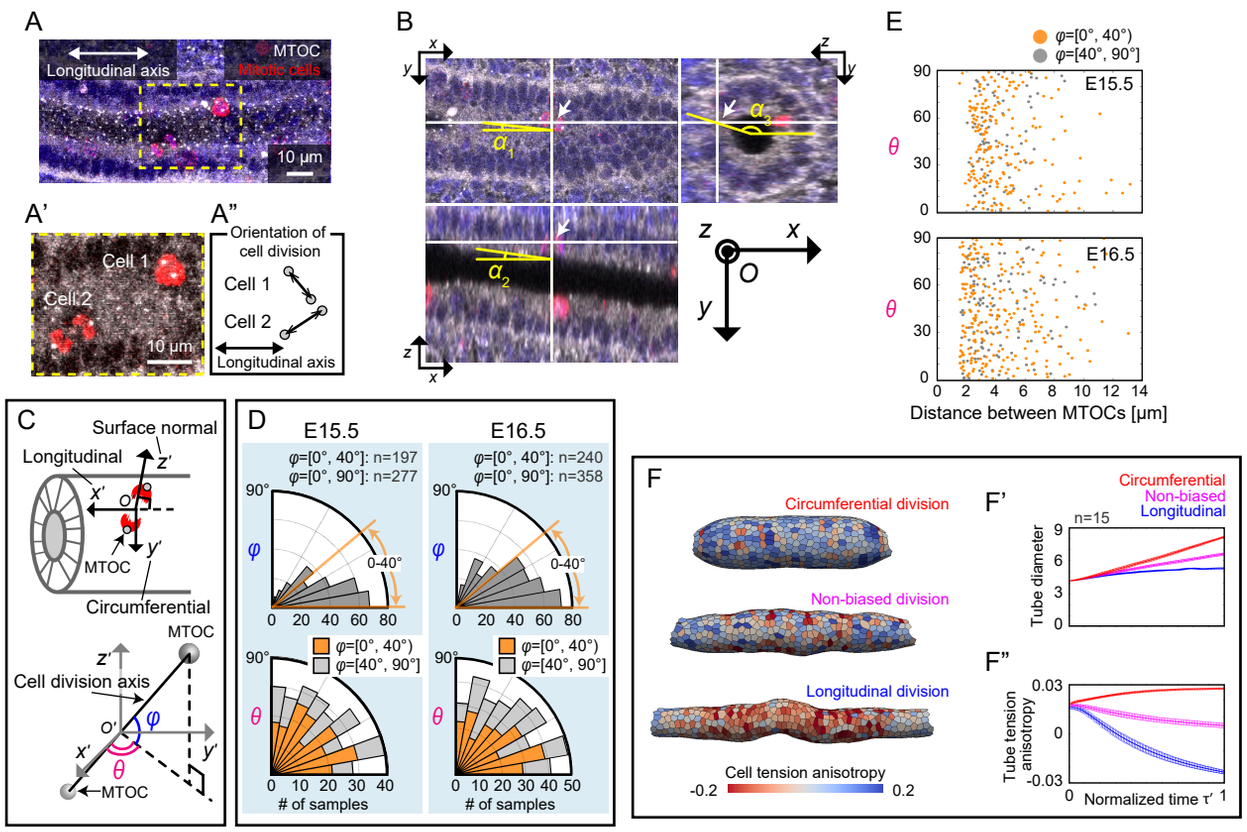
A
Longitudinal axis
MTOC
Mitotic cells
10 μm
A'
Cell 1
Cell 2
10 μm
A"
Orientation of cell division
Cell 1
Cell 2
Longitudinal axis
B
E
φ=[0°, 40°)
φ=[40°, 90°]
E15.5
E16.5
θ
Distance between MTOCs [μm]
C
Surface normal
Longitudinal
Circumferential
MTOC
Cell division axis
D
E15.5
E16.5
φ=[0°, 40°]: n=197
φ=[0°, 90°]: n=277
φ=[0°, 40°]: n=240
φ=[0°, 90°]: n=358
0-40°
# of samples
F
Circumferential division
Non-biased division
Longitudinal division
Cell tension anisotropy
-0.2
0.2
F'
Circumferential
Non-biased
Longitudinal
n=15
Tube diameter
F"
Tube tension anisotropy
Normalized time τ'

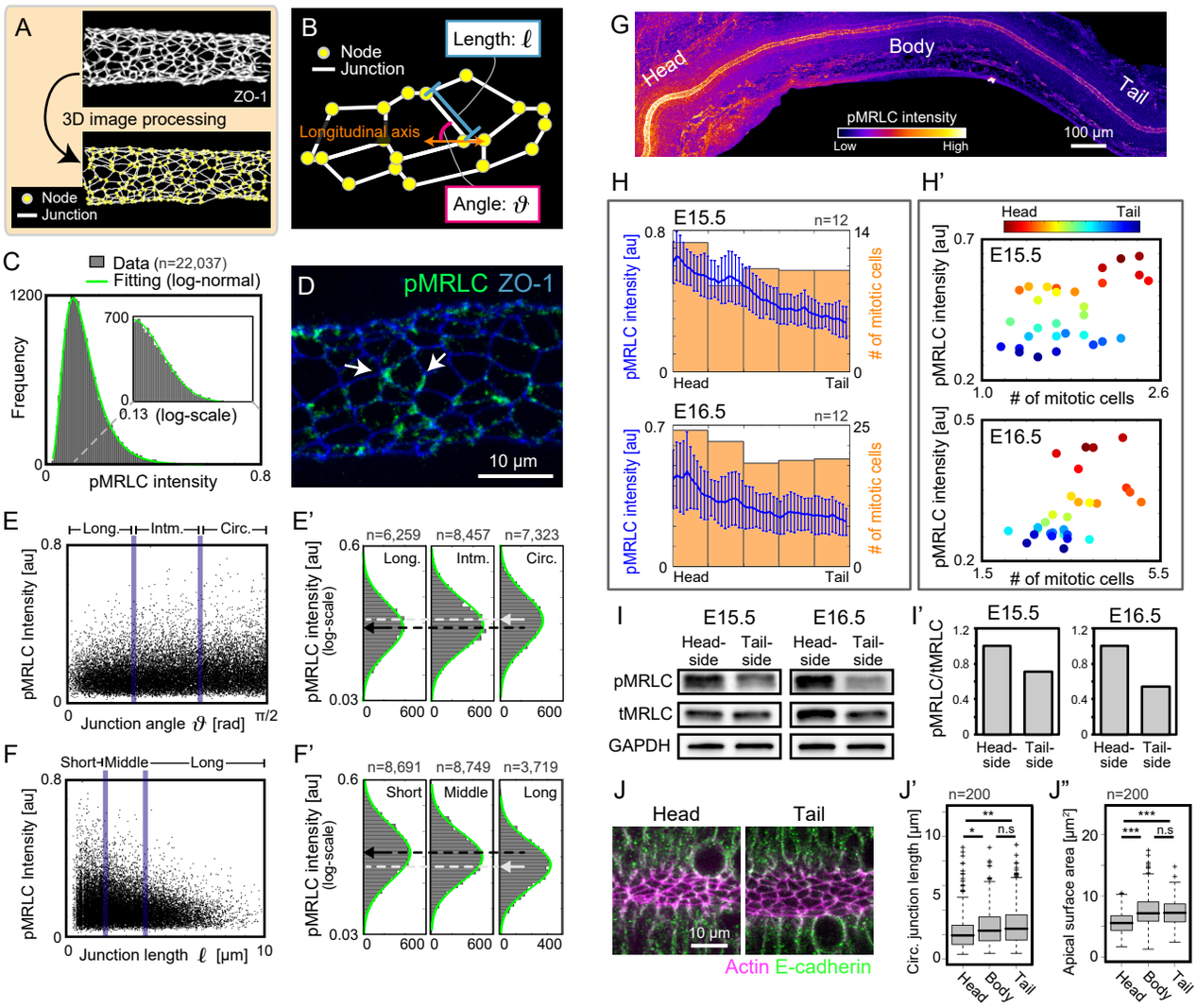
A
ZO-1
3D image processing
Node
Junction
B
Node
Junction
Length: ℓ
Longitudinal axis
Angle: ϑ
C
Data (n=22,037)
Fitting (log-normal)
Frequency
pMRLC intensity
0.13 (log-scale)
D
pMRLC ZO-1
10 μm
E
Long.
Intm.
Circ.
pMRLC Intensity [au]
Junction angle ϑ [rad]
E'
n=6,259
n=8,457
n=7,323
pMRLC intensity [au] (log-scale)
F
Short
Middle
Long
Junction length ℓ [μm]
F'
n=8,691
n=8,749
n=3,719
G
Head
Body
Tail
pMRLC intensity
Low
High
100 μm
H
E15.5
E16.5
n=12
pMRLC intensity [au]
# of mitotic cells
Head
Tail
H'
E15.5
E16.5
# of mitotic cells
I
E15.5
E16.5
Head-side
Tail-side
pMRLC
tMRLC
GAPDH
I'
pMRLC/tMRLC
J
Head
Tail
10 μm
Actin E-cadherin
J'
n=200
Circ. junction length [μm]
n.s
J"
Apical surface area [μm²]

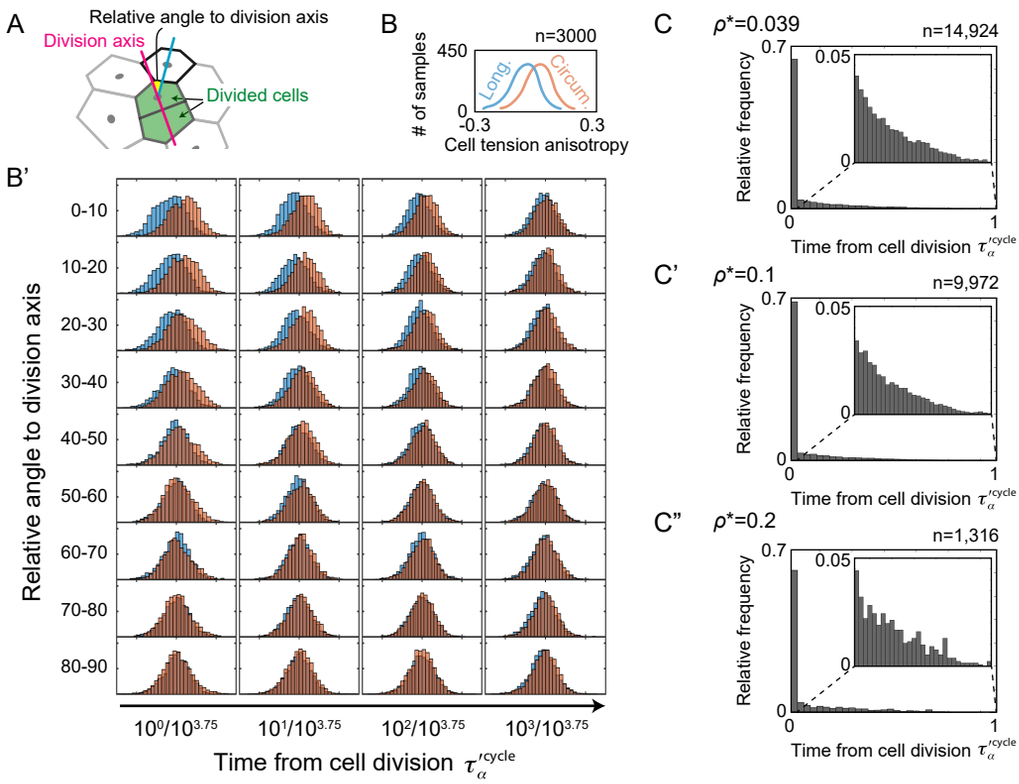
A
Relative angle to division axis
Division axis
Divided cells
B
n=3000
450
0
# of samples
Long.
Circum.
-0.3
0.3
Cell tension anisotropy
B'
0-10
10-20
20-30
30-40
40-50
50-60
60-70
70-80
80-90
Relative angle to division axis
$10^0/10^{3.75}$
$10^1/10^{3.75}$
$10^2/10^{3.75}$
$10^3/10^{3.75}$
Time from cell division $\tau_\alpha'^{cycle}$
C
ρ^*=0.039
n=14,924
0.7
0.05
0
Relative frequency
0
1
Time from cell division $\tau_\alpha'^{cycle}$
C'
ρ^*=0.1
n=9,972
C"
ρ^*=0.2
n=1,316

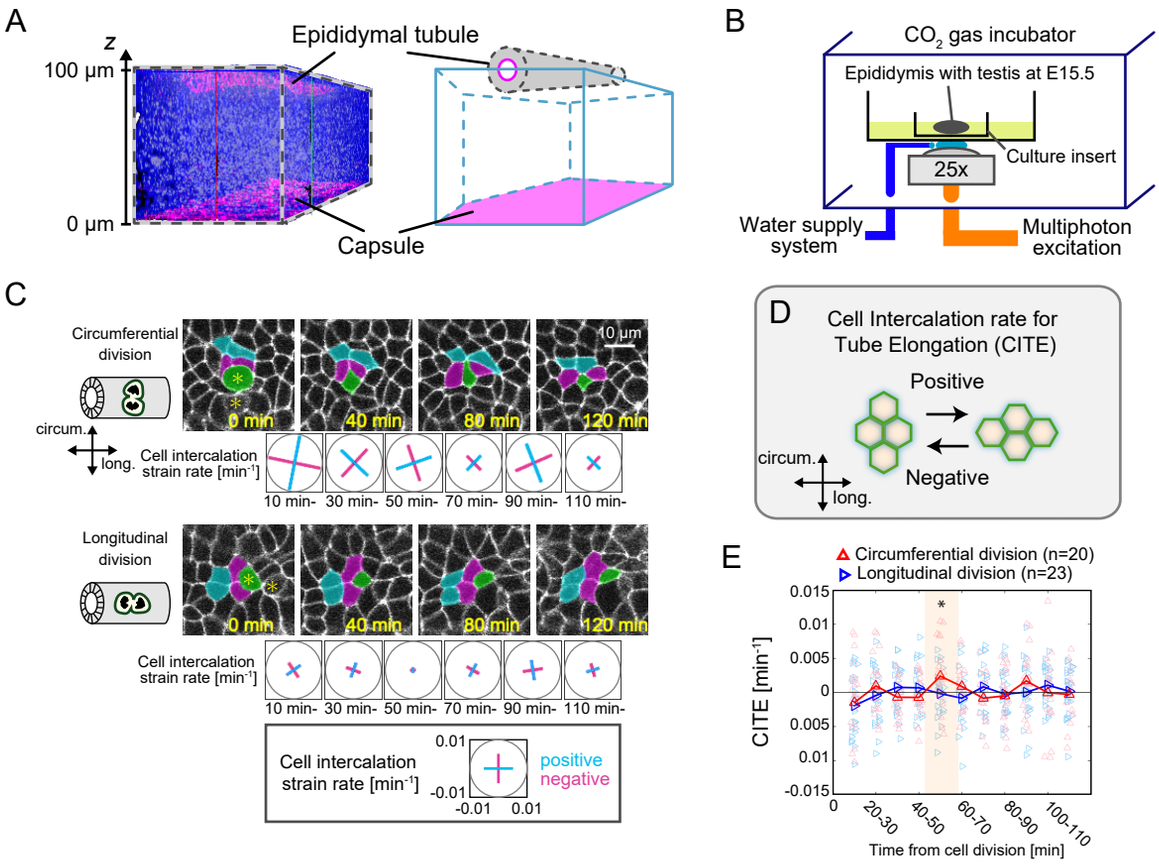
A
z
100 µm
0 µm
Epididymal tubule
Capsule
B
CO2 gas incubator
Epididymis with testis at E15.5
Culture insert
25x
Water supply system
Multiphoton excitation
C
Circumferential division
circum.
long.
Cell intercalation strain rate [min-1]
10 µm
0 min
40 min
80 min
120 min
10 min-
30 min-
50 min-
70 min-
90 min-
110 min-
Longitudinal division
Cell intercalation strain rate [min-1]
0.01
-0.01
-0.01
0.01
positive
negative
D
Cell Intercalation rate for Tube Elongation (CITE)
Positive
Negative
circum.
long.
E
Circumferential division (n=20)
Longitudinal division (n=23)
CITE [min-1]
0.015
0.01
0.005
0
0.005
0.01
-0.015
0
20-30
40-50
60-70
80-90
100-110
Time from cell division [min]

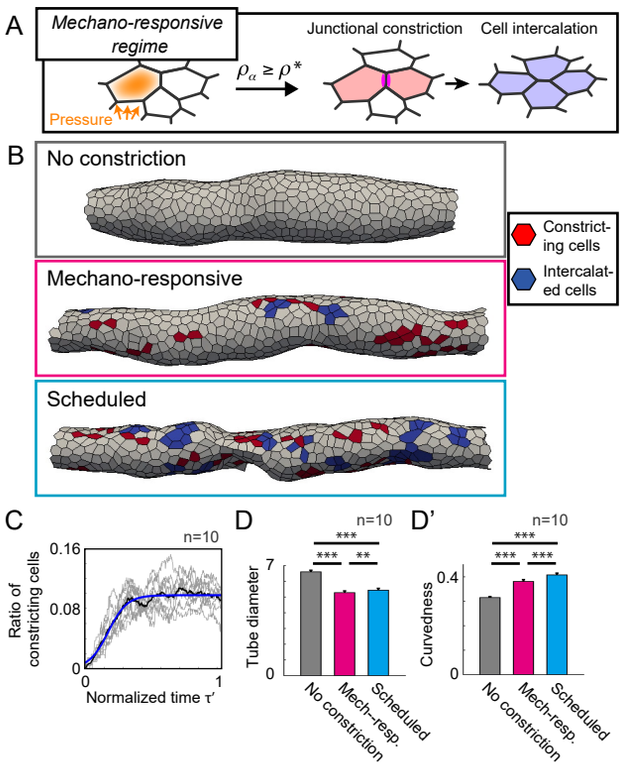
A
Mechano-responsive regime
Pressure
$\rho_\alpha \geq \rho^*$
Junctional constriction
Cell intercalation
B
No constriction
Mechano-responsive
Scheduled
Constrict-ing cells
Intercalat-ed cells
C
n=10
Ratio of constricting cells
0.16
0.08
0
0
1
Normalized time τ'
D
n=10
Tube diameter
7
0
***
***
**
No constriction
Mech.-resp.
Scheduled
D'
n=10
Curvedness
0.4
0
***
***
***
No constriction
Mech.-resp.
Scheduled

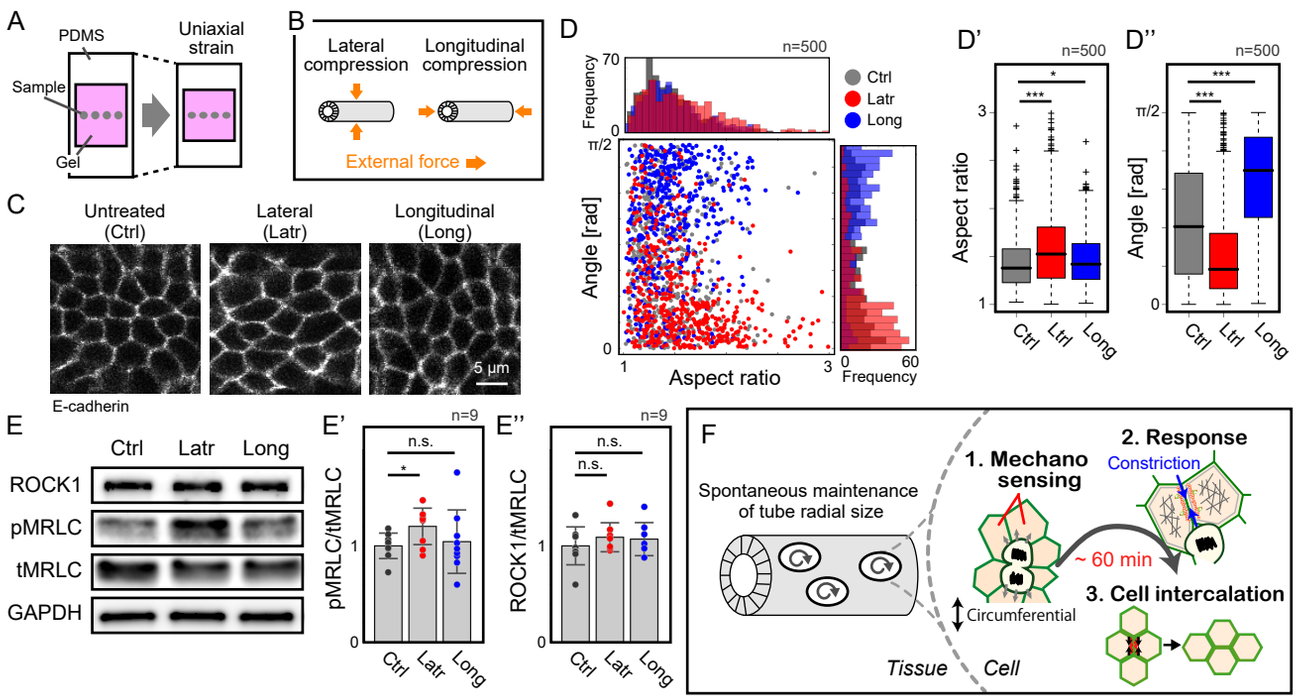
A
PDMS
Uniaxial strain
Sample
Gel
B
Lateral compression
Longitudinal compression
External force
C
Untreated (Ctrl)
Lateral (Latr)
Longitudinal (Long)
5 μm
E-cadherin
D
n=500
Frequency
Ctrl
Latr
Long
Angle [rad]
Aspect ratio
D'
D''
Aspect ratio
Angle [rad]
E
Ctrl
Latr
Long
ROCK1
pMRLC
tMRLC
GAPDH
E'
E''
n=9
n.s.
pMRLC/tMRLC
ROCK1/tMRLC
F
Spontaneous maintenance of tube radial size
1. Mechano sensing
2. Response
Constriction
~ 60 min
3. Cell intercalation
Circumferential
Tissue
Cell